City Research Online

City, University of London Institutional Repository

Shear Connection of Prefabricated Ultra-Lightweight Concrete Slab Systems (PUSS™)

[1]Inas Mahmood Ahmed and [*2]Konstantinos Daniel Tsavdaridis

[1]Lecturer of Structural Engineering, Northern Technical University, Mosul, Iraq

[2]Professor of Structural Engineering, Department of Civil Engineering, School of Mathematics, Computer Science and Engineering, City, University of London, Northampton Square, EC1V 0HB, London, UK

[*]*Corresponding author* (konstantinos.tsavdaridis@city.ac.uk)

ABSTRACT

This paper reports a detailed numerical (FE) study of a recently developed novel steel-concrete composite flooring system (PUSS) with two different types of shear connectors web-welded shear stud connectors (WWSS) and web-welded shear stud with dowels (WWSS with dowels) as well as different types of concrete using normal and lightweight concrete. A nonlinear FE model is developed and validated against two sets of full-scale push-out tests on the novel steel-concrete composite flooring system reported in the companion paper. The FE model replicated the experimentally determined failure loads, ultimate slips and observed failure modes. Parametric studies are conducted to obtain failure loads and ultimate slips characteristics of this recently developed flooring system with different types of concrete: normal weight concrete, light weight concrete and ultra light weight concrete (NWC, LWC and ULWC), diameter, and height of shear connectors (WWSS, WWSS with dowels). The concrete strength of all types of concrete varied between 20 N/mm^2 to 35 N/mm^2 and the shear connectors' diameter varied between 16 mm, 19 mm, 20 mm and 22 mm and the height of the shear studs between 75 mm and 100 mm. The load-slip curves obtained from the FE parametric

studies demonstrated that the FE models with the same diameter had different slip stiffness, where the failure loads and slips varied with the concrete strengths. The slip results were also compared with different shear connection systems' dimensions at concrete strengths of 20, 30 and 35 N/mm^2.

1. INTRODUCTION

In the companion paper [1] the authors have reported eight full scale tests on novel steel-concrete composite flooring system (PUSS). The details of the tests including general setup and instrumentation, load-slip response, shear strength, ultimate failure load, failure modes and behaviour of the shear connection systems designed for PUSS have been disclosed [2-12]. Based on the obtained results, the compressive strength of the concrete significantly influences the ultimate shear strength capacity loads while it is influencing the failure mode of the shear connection system.

The novel steel-concrete composite flooring system (PUSS) consists of two main structural components: the concrete floor and the steel beams. The concrete floor is in the form of T-ribbed slab sections constructed using reinforced lightweight aggregate concrete. The C-channel steel edge beams encapsulate the floor slab and provide clean and straight finish edges. The floor slab width is 2.0 m inclusive of the width of the steel edge beams and a finished depth of 230 mm [1]. The total weight of the floor is reduced by having ribs and troughs running from one side to the other side of the slab sitting on the two C-channel edge beams either side. This ultra-shallow flooring system also reduces the weight and the number of erection

(installation) lifts by using lighter elements (lightweight concrete and thin-walled steel elements) and the wider possible units. Moreover, the extent of onsite works is reduced by offsite fabrication as the material cost against the fabrication and site erection costs is proportional in the order of 35% and 65%, respectively [2, 3]. In addition, this new flooring system can be used with slimflor and ultra-shallow floor beams, creating a shallow floor construction system.

Numerical and FE analyses are alternative methods in investigating the structural behaviour of novel steel-concrete composite flooring system (PUSS). The FE analysis has the advantages of lower time consumption with lower cost and higher efficiency. The accuracy and reliability of the FE analysis have been demonstrated by many researchers in the past. For composite flooring systems with shear connection interaction, various FE models have been proposed. Veljkovic [13] performed 3D FE analysis using software DIANA to investigate the behaviour of steel concrete composite slabs, where the shear connection between the steel deck and the concrete was modelled using a nodal interface element. Easterling [14] also developed a procedure to generate the shear bond property from bending tests. The shear bond property or shear bond-slip curves were then applied to connector elements within the FE models to simulate the horizontal shear in the composite slabs. Daniels and Crisinel [15] developed a FE procedure using the plane beam elements to analyse single and continuous span composite slabs, in which the nonlinear behaviour of the materials was well considered. Abdullah and Widjaja [16] used two parallel Euler–Bernoulli beam elements to simulate the bending test of composite slab, but only one single typical longitudinal slice of the slab was considered in the model, and the vertical nodal displacements of the two parallel beam elements were forced to be the same. Tsalkatidis and Avdelas [17] also proposed a model where the shear bond

mechanism at the contact interface of the composite slabs was treated as a unilateral contact problem and simplified as a two-dimensional contact model. Ferrer et al. [18] simulated the pull-out tests of composite slabs using the FE method, in which the contact elements were implemented between the steel deck and the concrete, and various coefficients of friction were analyzed.

This paper is examining numerically the response of the push-out tests of the prefabricated ultra-shallow flooring system under static monotonic loads. The investigated parameters were the three different types of concrete: normal weight concrete, light weight concrete and ultra light weight concrete (NWC, LWC and ULWC), the diameter and the height of the web-welded shear stud connectors (WWSS) and web-welded shear stud with dowels (WWSS, WWSS with dowels). A total of 84 parametric studies have been carried out to further verify the empirical formula (Eq. 16) obtained from the mathematical analysis in the companion paper [1]. The results of the FEA parametric studies were compared with the calculated shear resistance using the developed formula (Eq. 16) in [1].
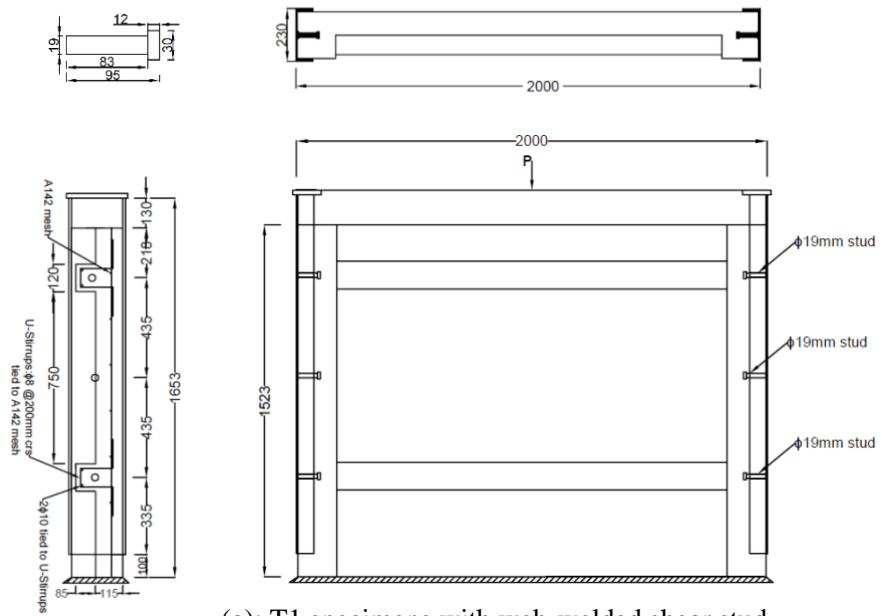
(a): T1 specimens with web-welded shear stud
connectors (WWSS) [1]
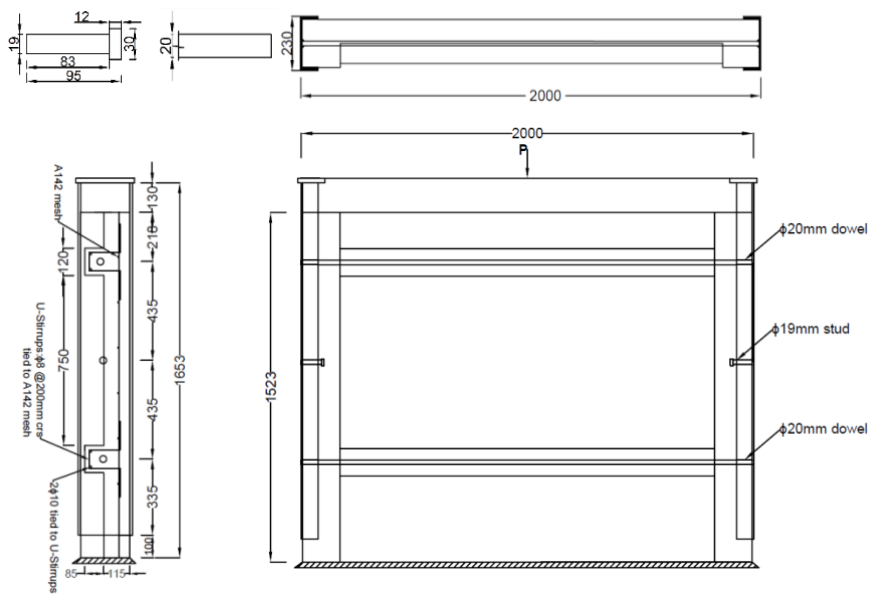
(b): T2 specimens with web-welded shear stud connectors
with dowels shear connectors (WWSS with dowels) [1]

Fig. 1. Details of the tested Specimens

2. FINITE ELEMENT MODELLING

The three dimension (3-D) finite element models of the push-out test of the prefabricated ultra-shallow flooring system investigated experimentally in the companion paper [1] were developed using the finite element software ABAQUS 6.14 [19]. The geometry of the simulated prefabricated ultra-shallow flooring system is shown in Fig.1, which were validated against the models results. The parameters adopted in the parametric studies were described herein.

2.1 FE model development

2.1.1   Analysis method

The RIKS method is frequently used to study the behaviour of the shear connectors in the push-out test [20]. The RIKS method is generally used to predict the unstable and nonlinear collapse of a structure. It is an implicit load control method. In the RIKS method, the load is applied proportionally in several load steps. In each load step, the equilibrium iteration is performed and the equilibrium path is tracked in the load-displacement space. The displacement control is applied. Loading is downward enforced displacement applied to the top surface of the steel beam, as shown in Fig.17(b) in section 2.1.3. This method is often used in static analysis and has been shown to be a strong method for nonlinear analysis. However, due to the equilibrium iteration, the RIKS method consumes much time and computer resources for a relatively large model. In addition, the convergence problem is often encountered when material damage and failure are included, and thus the ultimate load could not be obtained.

In this study, the dynamic explicit analysis method is used, which is a time control method. It is usually used for problems relating to metal forming, impact and progressing damage and failure of the material. It has been shown to be an efficient solution scheme for contact interaction, discontinuous mediums and large deformations. It has been used in many problems such as metal sheet forming [21], crack and failure of concrete material [22] composite laminate impact [23], among others. Despite being a dynamic method, the dynamic explicit analysis is also used for quasi-static analyses.

The size of the time increment is specified according to the mesh size and material properties. The time of the analysis can be reduced by using mass scaling. The explicit analysis is very efficient for solving contact and discontinuous problems; therefore, it is adequate for the simulation of push-out test. It can be used for the simulation of the push-out test with the same loading rate as in the real experiment. Nevertheless, in order to reduce the time of analysis, the approach of increasing loading rate is used in this study. Different loading rates were used and the most appropriated rate was determined as 0.25 mm/s.

2.1.2 Material properties

The components of the prefabricated ultra-shallow flooring system that were simulated using the dynamic explicit analysis method, include the steel beam, the concrete slab, the shear connectors, the steel reinforcement and the base block. Surface-based contact was used for modelling the contact interface between the steel beam and the concrete slab. The concrete damaged plasticity model is used in the current study for representing the behaviour of all types of concrete including the lightweight and ultra-lightweight concrete.

The concrete damaged plasticity model uses isotropic damaged elasticity in combination with isotropic tensile and compressive plasticity. This option in ABAQUS is used to define yield function, flow potential and viscosity parameters. This concrete model follows the non-associated plasticity flow rule, using the Drucker-Prager hyperbolic function for the flow potential. In the concrete damaged plasticity model, the plastic potential function and the yield surface do not coincide with each other. Concrete can show a significant volume change, commonly referred to as dilation, when subjected to severe inelastic stress states. This dilation can be represented by the appropriate plastic potential function. Conversely, the yield surface can be defined by the hardening rule. In this study, the dilation angle is taken as 38°. The material dilation angle (ψ) and eccentricity (ε) were taken as 38, and 0.1, respectively. The ratio of biaxial compressive strength to uniaxial compressive strength (f_{bo}/f_{co}) is taken as 1.16. These default values have been used from Abaqus manual. The degradation of the stress-strain curves in compression for concrete, especially the light and ultra-light weight concrete, was not captured as the materials damaged before reaching that point. Therefore, the compression behaviour of the normal concrete is presented by an equivalent uniaxial stress-strain behaviour curve, as shown in Fig. 2, which is determined from Eq. 1 Eurocode 2 [24].

$$\frac{\sigma_c}{f_{cm}} = \left(\frac{k\eta - \eta^2}{1 + (k-2)\eta} \right) \tag{1}$$

Where:

σ_c : is the compressive stress of the normal concrete,

f_{cm}: is the characteristic compressive cylinder strength of normal concrete,

$f_{cm} = f_{ck} + 8$

$$\eta = \frac{\varepsilon_c}{\varepsilon_{c1}}$$

ε_{c1}: is the compressive strain of the normal concrete at the peak stress f_c,

$$\varepsilon_{c1} = 0.7 f_{cm}^{0.31} \leq 2.8$$

$$k = \frac{1.05 E_{cm} \times |\varepsilon_{c1}}{f_{cm}}$$

$$E_{cm} = 22 \times \left(\frac{f_{cm}}{10}\right)^{0.3}$$

The expression 1 is valid for $0 < |\varepsilon_c| < |\varepsilon_{cu1}|$ where ε_{cu1} is the nominal ultimate strain. The nominal ultimate strain, ε_{cu1} for concrete characteristic compressive cylinder strength of 12–50 MPa can be taken as 0.0035 Eurocode 2 [24]. For a characteristic compressive strength greater than 50MPa, the ultimate compressive strain can be calculated from the following expression.

$$\varepsilon_{cu1} = 2.8 + 27 \left[\frac{(98 - f_{cm})}{100}\right]^4 \qquad (2)$$
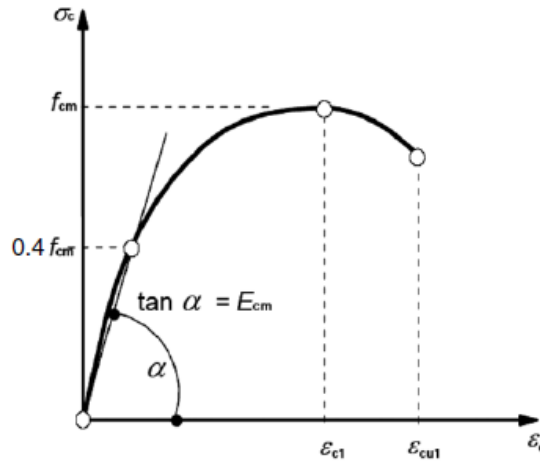
Fig. 2: Schematic of the stress–strain relation for concrete material Eurocode 2 [24]

Stiffness degradation on account of crushing the concrete is assumed to be zero. Consequently, no compression damage data is specified in the input. According to the ABAQUS manual [25], in the absence of compression damage, the plastic strain of concrete can be taken as equal to the inelastic strain. The uniaxial stress-plastic strain curve for the push test specimen, with a mean compressive cylinder strength, f_{cm} of 38.8 MPa, is shown in Fig. 3.
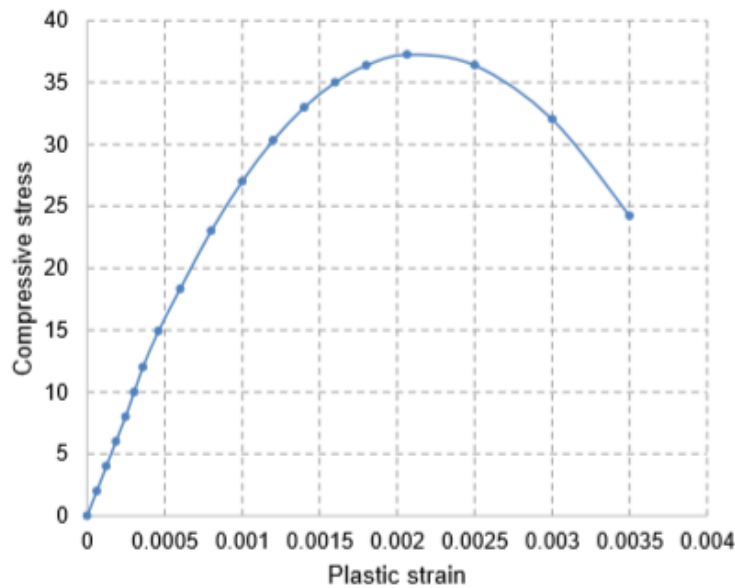
Fig. 3: Stress-strain curve in compression for normal concrete material

For concrete in tension, the tensile stress is assumed to increase linearly with respect to strain, until the concrete crack occurs. After the crack, the tensile stress decreases to zero with the tension stiffening effect. Tension stiffening can be defined by means of a post-failure stress-strain relationship, or by applying a fracture energy cracking criterion. As mentioned in the ABAQUS manual [25], in cases with little or no reinforcement, the stress-strain tension stiffening approach often causes mesh-sensitive results. Consequently, the fracture energy cracking criterion is used in this study. In this approach, the brittle behaviour of concrete is represented by a stress displacement response, rather than a stress-strain response.

Different methods can be used to define the brittle behaviour of concrete using the fracture energy concept. The most appropriate approach is to define tensile cracking using a linear approximation, in which the linear loss of strength takes place after cracking, as presented in Fig. 4(a). The brittle behaviour of concrete in tension can be expressed in a more detailed approach using a bilinear function, as established by Hillerborg [26], and shown in Fig. 4(b). A more accurate method of defining brittle behaviour is to use an exponential expression, which was experimentally established by Cornelissen et al. [27] and explained in Fig. 4(c), which can be calculated using the following Eques.

$$\frac{\sigma_t}{f_t} = f(w) - \frac{w}{w_c}f(w_c) \tag{3}$$

$$f(w) = \left[1 + \left(\frac{c_1 w}{w_c}\right)^3\right]\exp(-\frac{c_2 w}{w_c}) \tag{4}$$

Where:

w: is the crack opening displacement,

w_c: is the crack opening displacement at which stress can no longer be transferred $w_c = 5.14 G_f / f_t$ for normal weight concrete,

c_1: is a material constant and $c_1 = 3.0$ for normal weight concrete,

c_2: is a material constant and $c_2 = 6.93$ for normal weight concrete.

(a) Linear function   (b) Bilinear function   (c) Exponential function
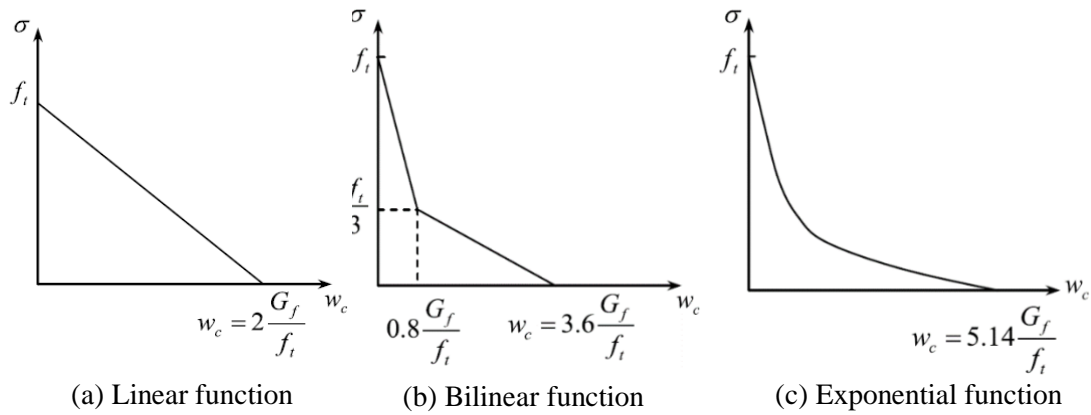
Fig. 4: Linear concrete tension softening model [25], Bilinear [26] and Exponential [27]

Concrete damage in tension is included in the material modelling. The elastic stiffness of the material is degraded when a concrete crack occurs. The degradation of the elastic stiffness is characterized by two damage parameters, d_c and d_t, which are assumed to be functions of the plastic strains. The damage parameters can take values from zero (representing the undamaged status) to 1 (representing the total loss of strength). It is observed from the experiment that the concrete cracking failure mode is dominant in the push–out test. Therefore, in the FE analysis, only the tension damage variable d_t is applied. Figs. 5 and 6 show tensile stress versus the cracking displacement curve and tensile damage against the cracking displacement curve for normal concrete material. The same formulas for representing normal concrete properties in tension and compression were used for the parametric study.
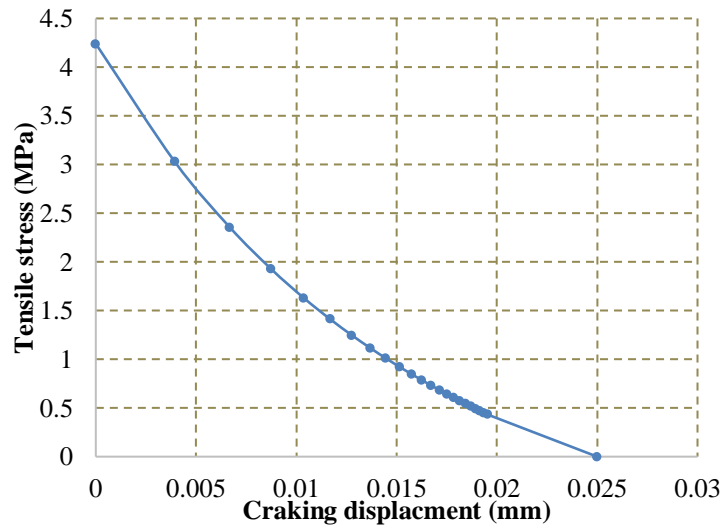
Fig. 5: Tensile stress versus cracking displacement curve
of normal concrete
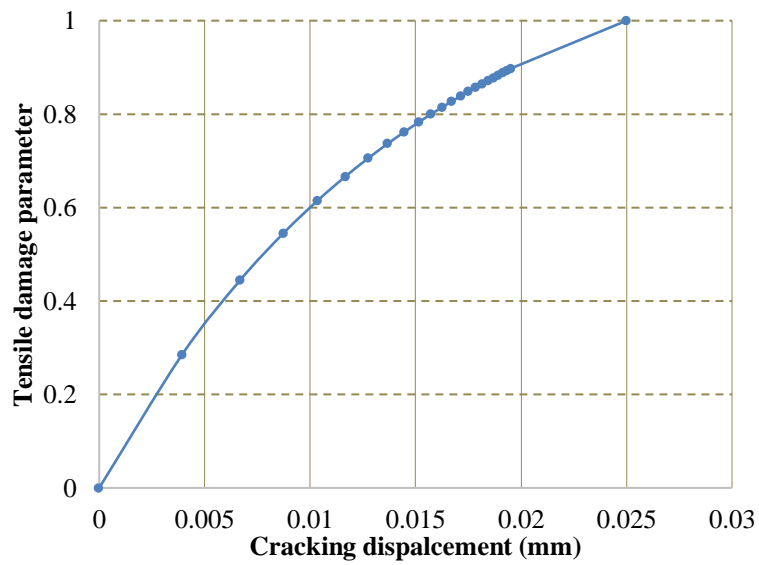
Fig. 6: Tensile damage versus cracking displacement curve
of normal concrete

The stress-strain behaviour in the compression of lightweight and ultra-lightweight concrete
are represented by a mathematical model established by (Almusallam and Alsayed) [28], which
is given by Eq. 5.

$$f_c = \frac{(K - K_p)\varepsilon_c}{\left[1 + \left(\frac{(K - K_p)\varepsilon_c}{f_0}\right)^n\right]^{1/n}} + K_p \varepsilon_c \qquad (5)$$

Where:

f_c is the concrete stress corresponding to the strain ε_c,

K: is the initial slope of the curve,

K_p, is the final slope of the curve,

f_o: is the reference stress,

n: is a curve-shape parameter.

These parameters are shown in Fig. 7.
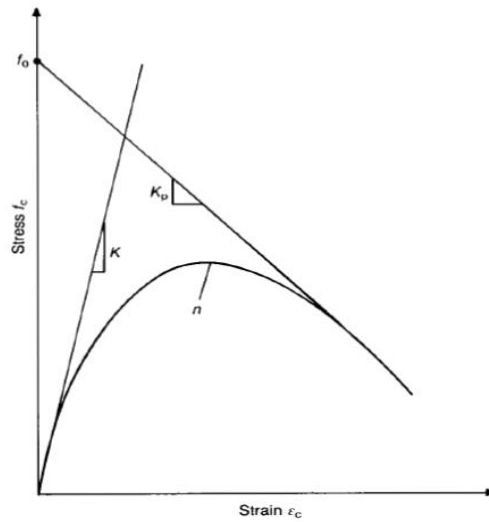
Fig. 7: Schematic of the stress-strain model showing its parameters [28]

$$n = -\frac{\ln 2}{\ln\left(\frac{f_1}{f_0} - \frac{K_p}{K - K_p}\right)} \qquad (6)$$

Where:

$$f_1 = f_c' \left[2\frac{\varepsilon_c}{\varepsilon_0} - \left(\frac{\varepsilon_1}{\varepsilon_0}\right)^2 \right] \tag{7}$$

$$\varepsilon_1 = \frac{0.65 f_0}{K - K_p} \tag{8}$$

$$f_0 = 19.1 + 1.3 f_c' - K_p \varepsilon_0 \tag{9}$$

$$K_p = 1374.5 - 871.1 f_c' \quad \text{for } f_c' \geq 15\text{MPa} \tag{10}$$

$$K = E_c = 180.9\, f_c' + 7770.7 \tag{11}$$

In addition, the relationship between the ultimate compressive strength and the corresponding strain is given by Eq. 12.

$$\varepsilon_0 = (0.398 f_c' + 18.147) \times 10^{-4} \tag{12}$$

Figs. 8 and 9 represent the stress-strain curves of lightweight concrete and ultra-lightweight concrete material in compression.
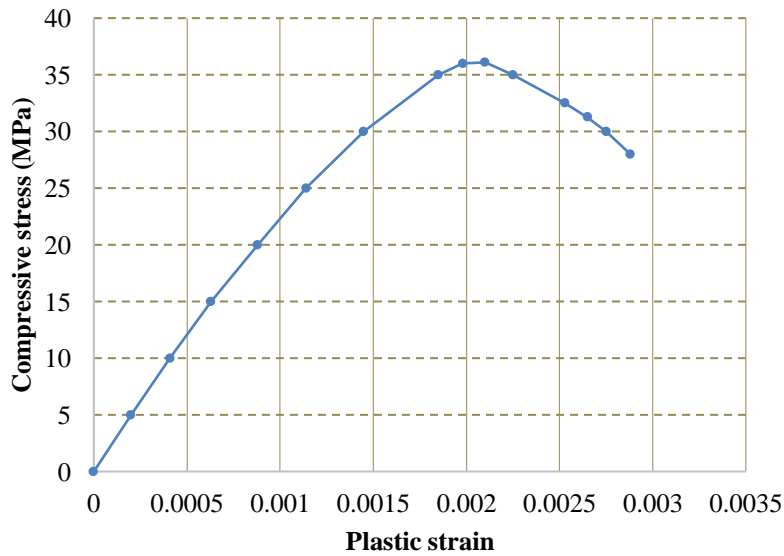
Fig. 8: Stress-strain curve in compression for lightweight concrete material
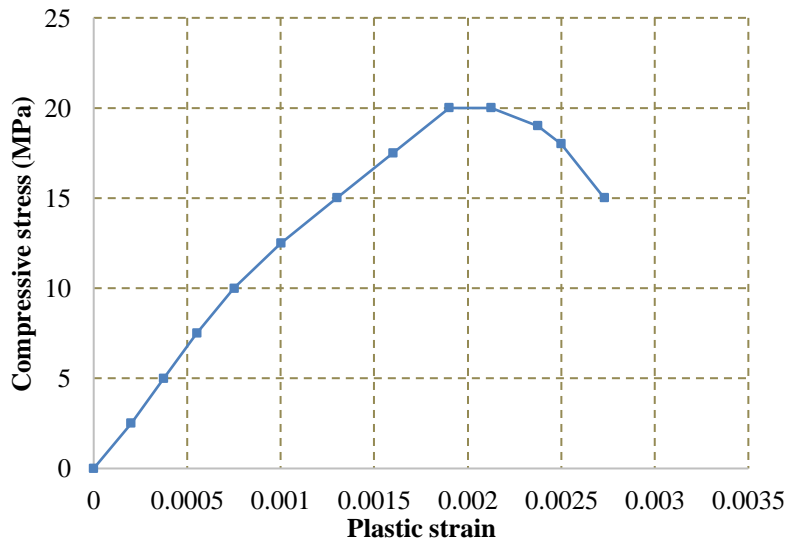
Fig. 9: Stress-strain curve in compression for ultra-lightweight
concrete material

The stress-strain curve in tension of lightweight concrete is presented by the mathematical

model [27] which is given by the following Eques.

$$\frac{\sigma_t}{f_t} = f(w) - \frac{w}{w_c} f(w_c) \tag{13}$$

$$f(w) = \left[1 + \left(\frac{c_1 w}{w_c}\right)^3\right] \exp(-\frac{c_2 w}{w_c}) \tag{14}$$

Where:

w: is the crack opening displacement,

w_c: is the crack opening displacement at which stress can no longer be transferred,

$w_c = 5.14 G_f / f_t$ for normal weight concrete,

c_1: is a material constant and $c_1 = 1$ for lightweight concrete,

c_2: is a material constant and $c_2 = 5.64$ for lightweight concrete.

Figs. 10 to 13 show tensile stress versus the cracking displacement curve and tensile damage

versus the cracking displacement curve of lightweight concrete and ultra-lightweight concrete

16

material in tension. The same formulas for representing lightweight and ultra-lightweight concrete properties in tension and compression were used for the parametric study.
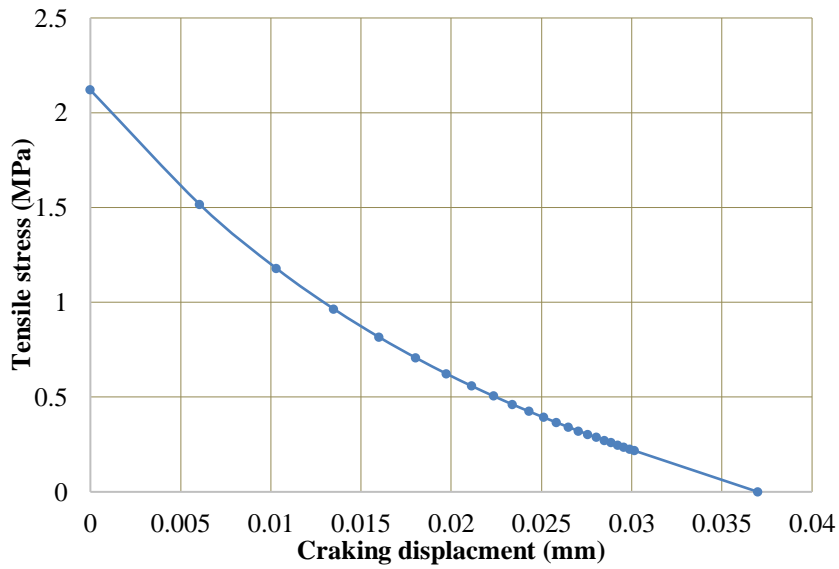
Fig. 10: Tensile stress versus cracking displacement curve of lightweight concrete material
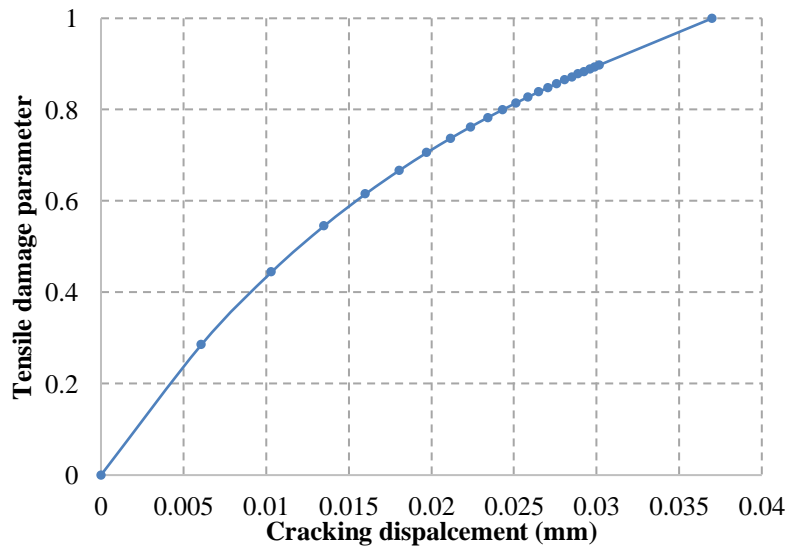
Fig. 11: Tensile damage versus cracking displacement curve of lightweight concrete material
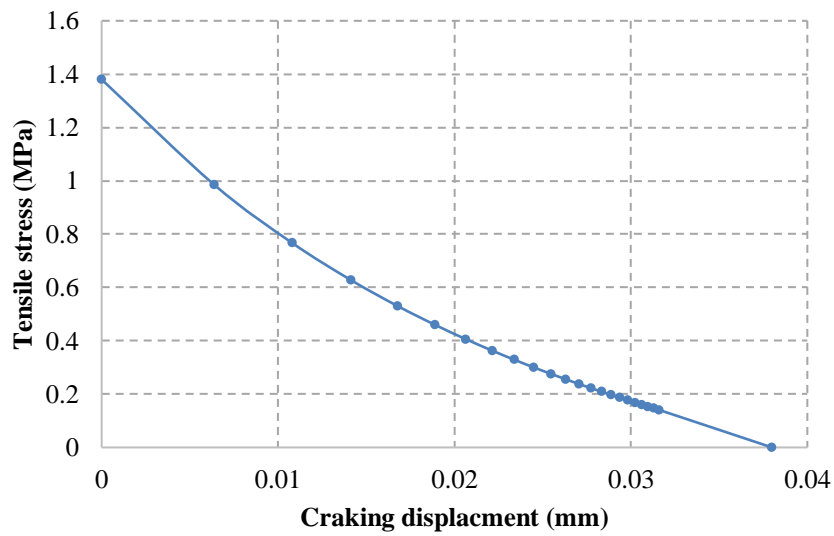
Fig. 12: Tensile stress versus cracking displacement curve of
ultra-lightweight concrete material
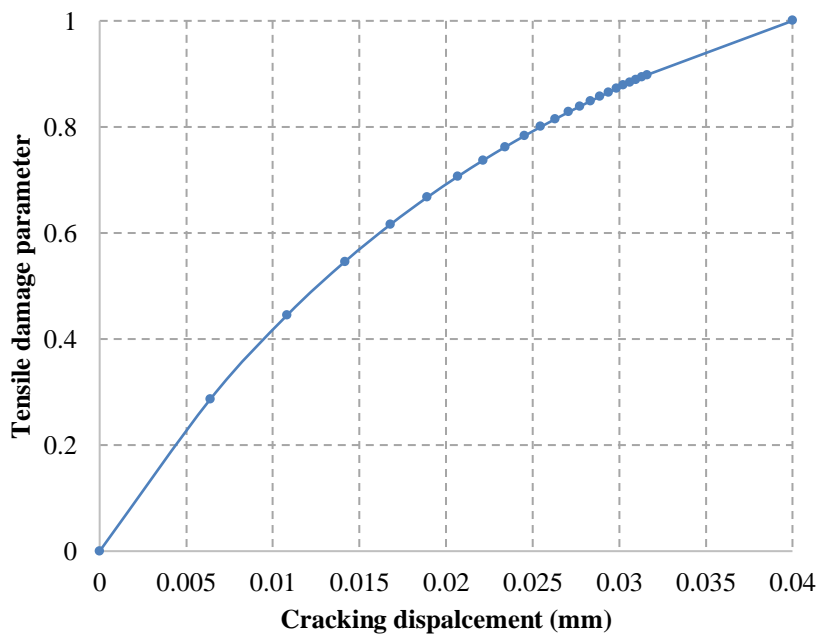
Fig. 13: Tensile damage versus cracking displacement curve of
ultra-lightweight concrete material

The material properties for the steel beam and reinforcing steel are other main components of
the model. The stress-strain curve for both steel beam and reinforcing steel can be obtained
from the steel tensile tests [29]. The data is input into two different material behaviours: elastic

and plastic options of the ABAQUS. Table 1 presents a summary of the steel components properties.

Table 1: Steel Components properties

Steel components	Yield Stress N/mm²	Yield Strain	Ultimate Strain
6 mm Steel Bar	550	0.0025	0.15
8 mm Steel Bar	598	0.0034	0.173
10 mm Steel Bar	503	0.0026	0.205
230x75x26 PFC	406	0.013	0.22
20 mm Steel Dowel	322.5	0.05	0.56
19 mm Steel Stud	421.0	0.0125	0.1125

The shear connectors material is of great importance in the model. The material is modelled by a trilinear stress-strain curve, as shown in Fig. 14 [30]. The behaviour of the shear connectors' material is initially elastic, followed by strain softening and then yielding. The yield stress (σ_{ys}) is determined at ε_{ys}=0.2% and the ultimate stress (σ_{us}) achieves ε_{us} =0.6%.
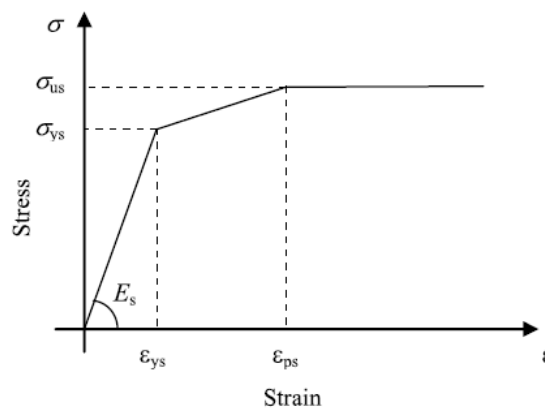
Fig. 14: Stress-strain relationship for shear connectors
[30]

For the headed shear stud connectors, the material properties presented by [31] are used for the FEA and parametric study. The steel dowels were tested in accordance with [29] and their

stress-strain curves were plotted. Similar to the structural steel, the material inputs of the shear studs were divided into elastic and plastic regions, based on the stress-strain relationship from the tests.

The material damage and failure options were used in the material model for the shear connection systems in order to achieve the exact load-slip relationship. Modelling the failure of the material requires two specifications: the damage initiation criterion and the damage evolution response. In general, the damage initiation criterion specifies a critical equivalent plastic strain, where the stiffness of the material starts to degrade, and the damage evolution describes how the stiffness of the material degrades.

As for the damage model of shear connection systems, the metal fracture strain is based on several factors, including strain rate, thermal effect, stress triaxiality, etc. Since the loading rate of 0.25 mm/s is considered slow enough to ignore the influence of strain rate and thermal effect, stress triaxiality is viewed as the primary factor. The relationship between stress triaxiality σ_m/σ_{eq} and the equivalent fracture strain P_R is expressed in Eq.15 [31], where ε_R refers to the fracture strain under uniaxial load; σ_m is the mean stress; σ_{eq} is the equivalent Mises stress; S_0 is a material constant with the same magnitude of 1, $S_0=1.5$, and v is the Poisson ratio.

$$P_R = \varepsilon_R \left[\frac{2}{3} + (1 + v) + 3(1 - 2v)\left(\frac{\sigma_m}{\sigma_{eq}}\right)^2 \right]^{S_o} \tag{15}$$

Additionally, it is assumed that the ratio of P_R to ε_R is approximately equal to the ratio of P_D to ε_D, where ε_D equals the uniaxial strain related to the onset of fracture, and P_D equals the spatial stress status of fracture initiation. Consequently, the relationship between P_D and ε_D is based on P_R and ε_R can be established. In the present study, the criterion of fracture initiation is used

as shown in Fig. 15. The exponential correlation between damage variable D and plastic displacement has been established based on [32]. The exponential law parameter is 0.01 and the equivalent plastic displacement is related to the dimension size of the discrete elements.
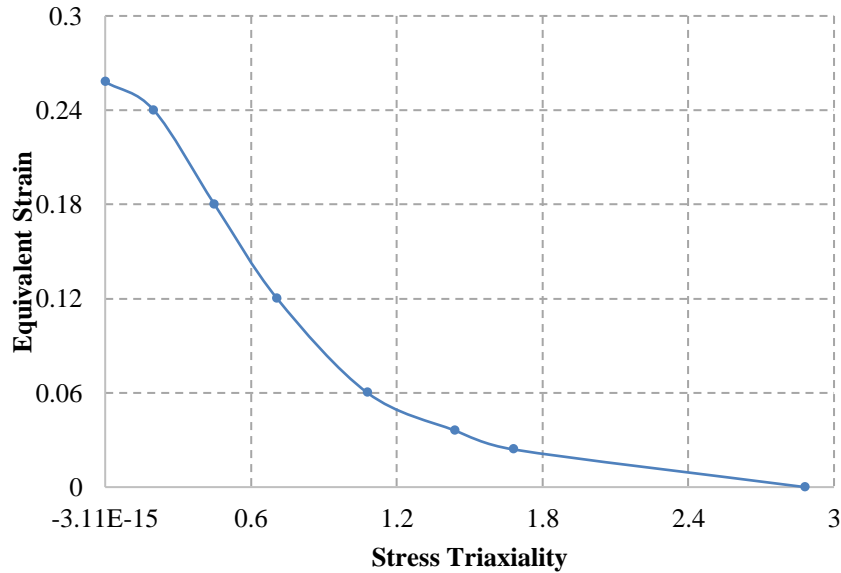
Fig. 15: Criterion of damage initiation of shear connection systems

2.1.3 Contact interaction and boundary conditions

Most of the contact problems are modelled using surface-based contact, therefore this is also used to simulate the contact interface between the concrete slab and the shear connection systems in this study. Since one of the objectives of this study is to investigate the behaviour of shear connection systems under longitudinal shear slip, the FE model must be able to model or consider the longitudinal interface slip of the shear connection systems. This is because the shear connection systems are stiffer than the concrete slab. Therefore, the surface of the shear connection systems is taken as a master surface, while the surface of the concrete slab is treated as a slave surface, as shown in Fig. 16(a). The interaction properties of the concrete slab and

shear connection systems surfaces are also defined by normal behaviour and are tangential to the surfaces. The penalty frictional formulation is used and the coefficient of friction between the steel beam and the concrete slab is taken as 0.5 [33]. Different values of the coefficient of friction were applied to find the appropriate value. In contrast, to prevent relative slip between the steel beam and the shear connection systems, the steel beams are merged with the dowel and headed shear stud connectors to form one part. This is equivalent to the actual push test experiments, where shear connectors remain tied to the steel beam by welding [30].

In addition, the surface-based contact is also used for modelling the contact interface between the steel beam and the concrete slab. In the push-out test, the steel beam surface contact with the concrete slab is usually greased to reduce friction. In the analysis, the frictionless contact pair algorithm is used to define surface-to-surface contact between the steel beam surfaces and the surfaces of the concrete slab, as shown in Fig.16(b). Generally, the harder material is selected as the master surface and the softer as a slave. The interaction properties of the steel beam and concrete slab surfaces are defined by normal behaviour and it is tangential to the surfaces. The default normal behaviour is assumed, which consists of a 'hard' contact pressure-over closure relationship. This type of normal behaviour allows for minimum penetration of the slave surface into the master surface. The penalty frictional formulation is used and the coefficient of friction between the steel beam and the concrete slab is taken as 0.0.

The contact interaction is also applied at the interface between the concrete slab and the base block, as shown in Fig.16(c). In this interaction, the friction coefficient is taken as 0.25, which is based on the study of [31].

22

However, the contact interface between the concrete and reinforcing steel is of less importance compared with the other interfaces. It is assumed that no slip takes place between the concrete slab and the reinforcing steel bars during the analysis. Therefore, the embedded constraint method is applied in the FE model, as shown in Fig.16(d). This embedded technique is used to specify the reinforcing bar elements that lie embedded in the host element, which in this case is the concrete slab that needs to be constrained. When a node of the reinforcing truss element lies within the host element, the degrees of freedom at the node are eliminated and the node becomes an "embedded node". The degrees of freedom of the reinforcing steel embedded node are constrained to the interpolated values of the degrees of freedom of the host element.

Due to the symmetry of the push-out test arrangement, the symmetric boundary condition (BC) is applied to the surfaces at the symmetric planes of the specimen. The axis symmetric BCs were applied to surface 1, as shown in Fig.17(a), for which the translational displacement U1 and rotational displacements (R2 and R3) of all nodes on surface 1, and U3 and the rotational displacements (R1 and R2) of all nodes on surface 1 were restrained. The base block is assumed to be immovable, so all DOF of the reference node of the base block is restricted.
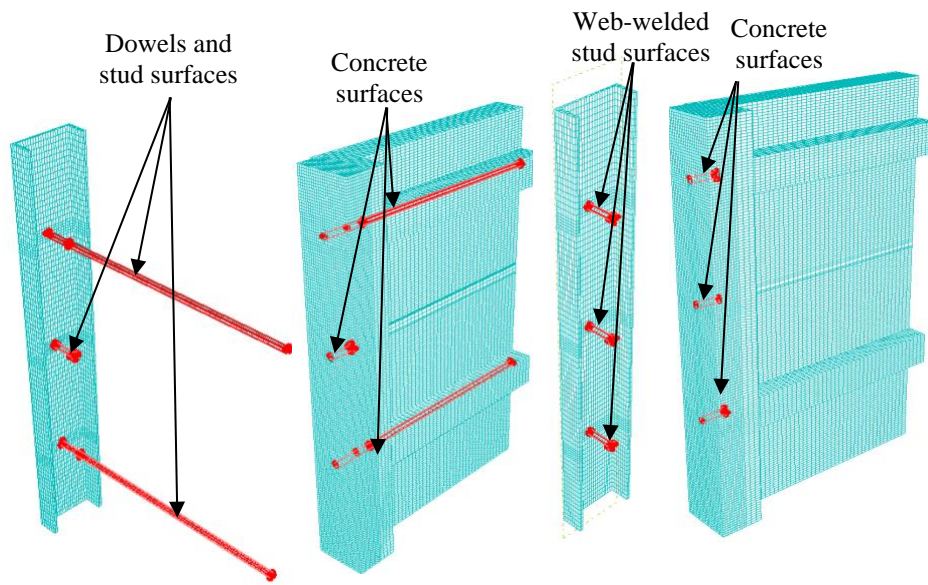
(a): Surfaces in tie constrain between concrete
and shear connection systems
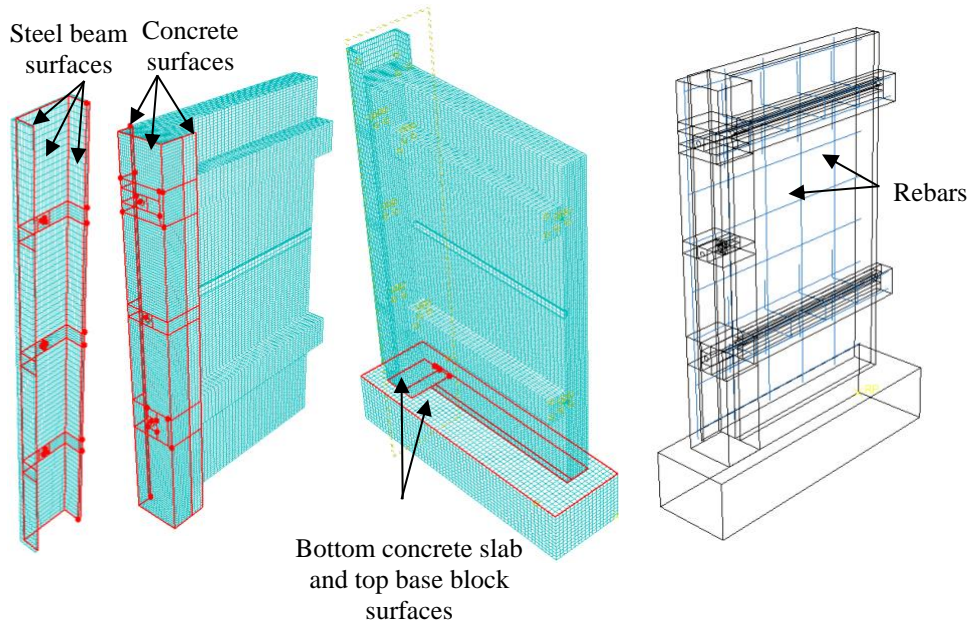
(b): Surfaces in contact interaction
between steel beam and concrete slab

(c): Surfaces in contact
interaction between concrete slab
and base block

(d): Rebars embedded
in concrete slab

Fig.16: Constrain and interaction surfaces

(a): Axis symmetric boundary condition (b): Base block boundary condition and loading surface
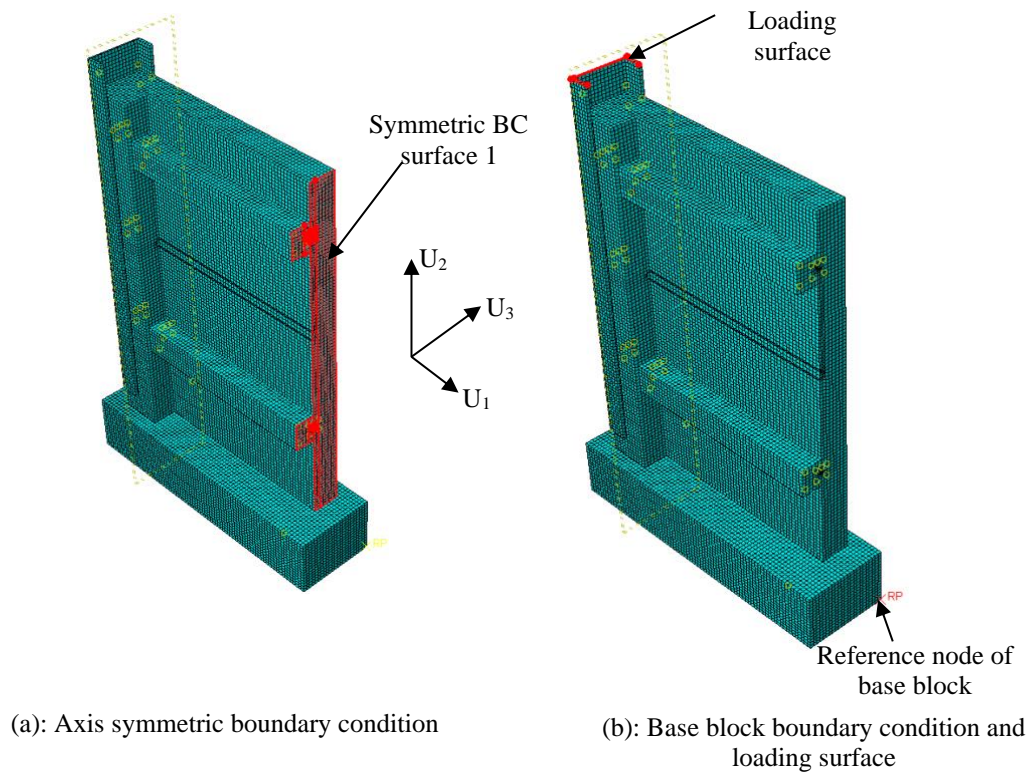
Fig.17: Boundary condition and loading surfaces

2.1.4 Mesh type

Due to the symmetry of the push-out test specimens, only half of the specimen with the three shear connectors was modelled. Fig.18(a) shows a full view of the specimen. The specimen is composed of six components: the concrete slab, steel channel, dowels, headed stud, reinforcing bars, reinforcing stirrups, and the mesh reinforcement. The components were modelled as separate parts, as presented in Fig.18(a).

In order to reduce the analysis time, a coarse mesh is applied to the overall size. The fine mesh is applied to the region around the interface between the concrete and the studs to achieve accurate results. In the headed stud, the mesh size is also reduced at the joint between the stud and steel beam where the stud would usually fail under shear force. A convergence sensitivity study was conducted to specify the best mesh size to be used (see section 3). The overall mesh

25

size is 20 mm and the smallest size is about 10mm. The finite element mesh of the specimen is presented in Fig.18(b).

The concrete slab, structural steel beam, and the shear connection systems parts, are modelled using a 3-D eight node element (C3D8R). This element type is an 8-node brick element with reduced integration stiffness. Each node has three translational degrees of freedom (DOF). Karlsson and Sorensen [34] illustrated how the solid elements can be used for both linear and complex nonlinear analysis, including contact, large deformation, plasticity and failure. For the reinforcing bars, reinforcing stirrups and reinforcing welded wire mesh parts, a 2-D two-node truss element (T3D2) with linear approximation of displacement, two nodes and three translational degrees of freedom were all used. However, 4-node block bilinear quadrilateral element (R3D4) were used to simulate the base block part.

Steel beam

Concrete ribbed slab

Base block

(a): A half of the push-out specimen

(b): Full view of the push-out specimen

Steel beam and shear connectors Element type C3D8R

Concrete slab Element type C3D8R

Base block Element type R3D4

Rebar Element type T3D2

(c): element types
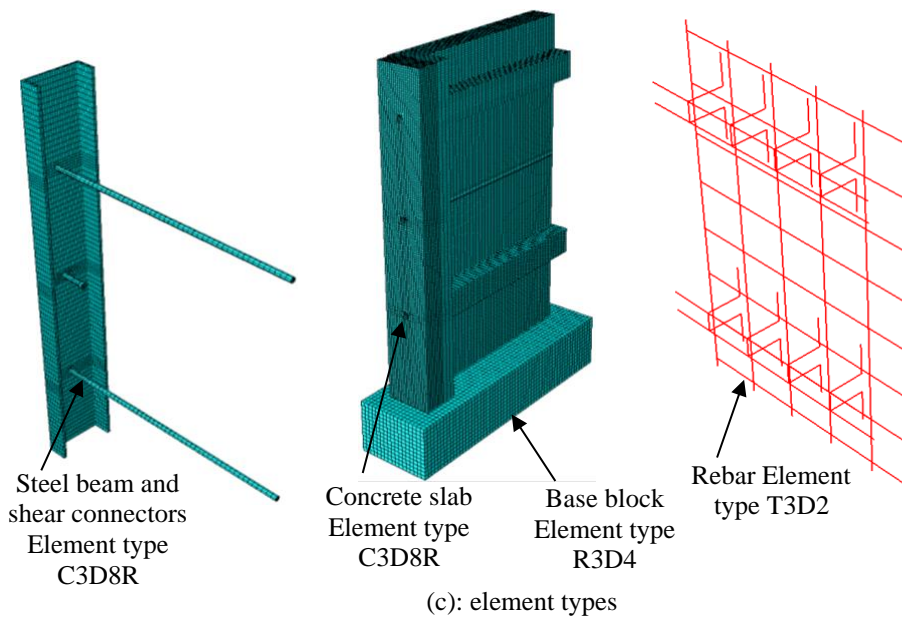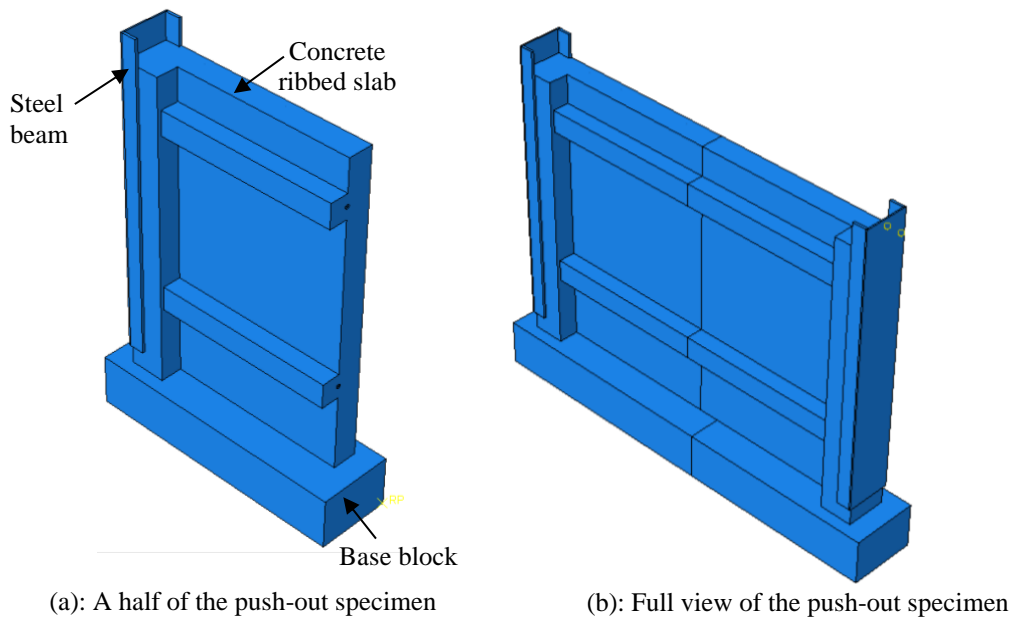
Fig.18: Finite element mesh type

2.1.5   Discretization of the mesh

A push-out test specimen with a shear connection system of dowels and studs is used to carry out the mesh convergence study (element size analysis). Only half of the specimen was modelled using the symmetric boundary conditions. Four different element sizes were used to determine the optimum size of the push-out test specimen for the FEA. The smallest three

element sizes were 15mm, 10mm and 8mm, with an overall mesh size of 20 mm. The normal weight concrete strength for the model is 37.3 MPa. A slip of 13.67 mm is applied to the model, which is the same slip obtained from push-out test specimen T2-NWC.

The load-slip of specimen T2-NWC and the models of different element sizes are shown in Fig.19. The summation of the measured reaction force on the loading surface at a slip of 6 mm Eurocode 4 [35] were compared between the models of different element sizes, as shown in Fig. 20. The results of the reaction force were almost identical between the models of element sizes (10 mm and 8 mm). Hence, these two element sizes could be used to model the FEA push-out tests. However, the computational time increases using the fine element size of 8 mm. Therefore, an element size of 10 mm was chosen as the optimum element size for the FEA push-out tests.

The slip has been measured in the experimental work using six digital dial gauges positioned on both sides of the slab. For the FEA the biggest slip value which obtained from the experimental work has been applied as a displacement at the top surface of the steel beam then the summation of the measured reaction force on the loading surface were obtained to draw the FEA load-slip curve.
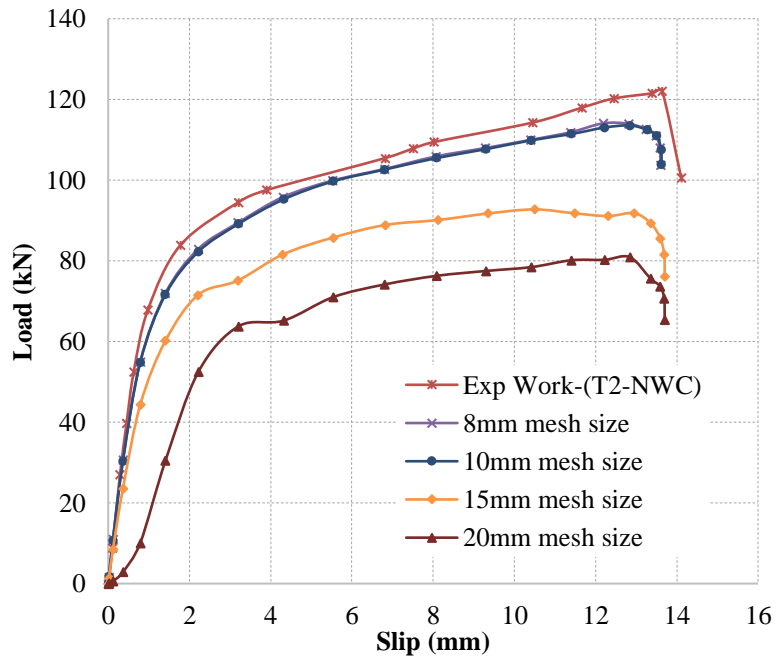
Fig.19: Load-slip of specimen T2-NWC and models with
different element sizes
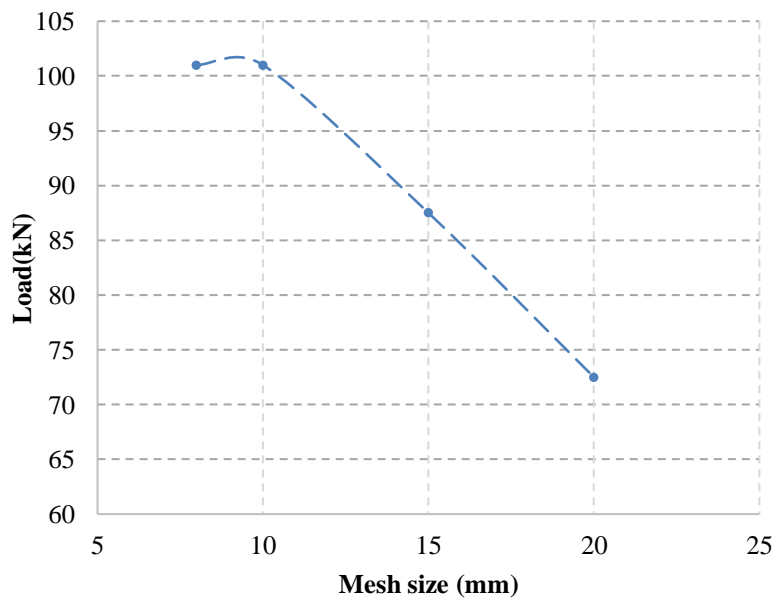
Fig. 20: Load-mesh size of models with different element size
at slip of 6 mm

3. VALIDATION STUDY

The FEA of the shear connection systems is carried out by using the material strengths obtained in the push-out tests. The results of the FEA were compared with the results of the push-out tests.

The comparisons for the failure loads and slip between the push-out tests and the FEA are summarised in Table 2. The identical slip stiffness between the results of the FEA and push-out tests are illustrated in Figs. 21 and 22. Both the failure loads and slips of the FEA were very close to those of the push-out tests. The average ratio for the failure loads between the results of the FEA and push-out tests is 1.06. The average ratio for the slips between the results of the FEA and push-out tests is 1.04.

It can be observed that the numerical load–slip behaviour resembles the experimental load slip behaviour reasonably well. The experimental as well as numerical results showed almost equivalent shear resistance per shear connection and maximum slip at failure. Although, the load–slip curve in finite element analysis followed a similar trend as that of the experimental curve, the former had a slightly lower falling branch than the latter. The difference between experimental and numerical load–slip curve in the post-failure range in Figs. 21 & 22. could be due to two reasons. First, the push test specimen was loaded under load control in experiments, which meant that as soon as the failure load was reached, there is always a slight tendency of overloading the specimen leading to a rapid drop in the load–slip curve. On the contrary, in finite element analysis; the model was loaded very slowly under displacement control by applying small velocity in increments. The way the load was applied to the specimen in experiment and numerical model could be the reason for the slight variation in load–slip behaviour in the post-failure range. Second, the concrete's compressive strength is modelled

in accordance to BS EN 1992-1-1 which might have a slight variation to the actual stress–strain characteristic of the concrete used in the experiment. Yet, in general, the finite element model effectively captured the load–slip behaviour of the push test experiment.

Table 2: Comparisons between the results of the push-out test specimens and FE models

Test Reference	Concrete strength fc (MPa)	Failure Load			Slip		
		Push-out test (kN)	FEA (kN)	Ratio (Test/FEA)	Push-out test (mm)	FEA (mm)	Ratio (Test/FEA)
T1-NWC	38.52	103.97	96.78	1.07	10.28	9.27	1.10
T1-LWC	32.20	86.70	78.75	1.10	19.98	17.90	1.11
T1-ULWC	20.0	57.02	55.74	1.02	20.15	19.45	1.03
T2-NWC	37.3	121.90	113.54	1.07	13.64	12.84	1.06
T2-LWC-1	34.6	101.65	95.46	1.06	20.45	20.04	1.02
T2-LWC-2	36.8	103.51	96.62	1.07	21.62	21.79	0.992
T2-ULWC	20.0	73.83	69.12	1.06	28.72	28.04	1.02
Mean				1.064			1.047
CV				2.23			4.22
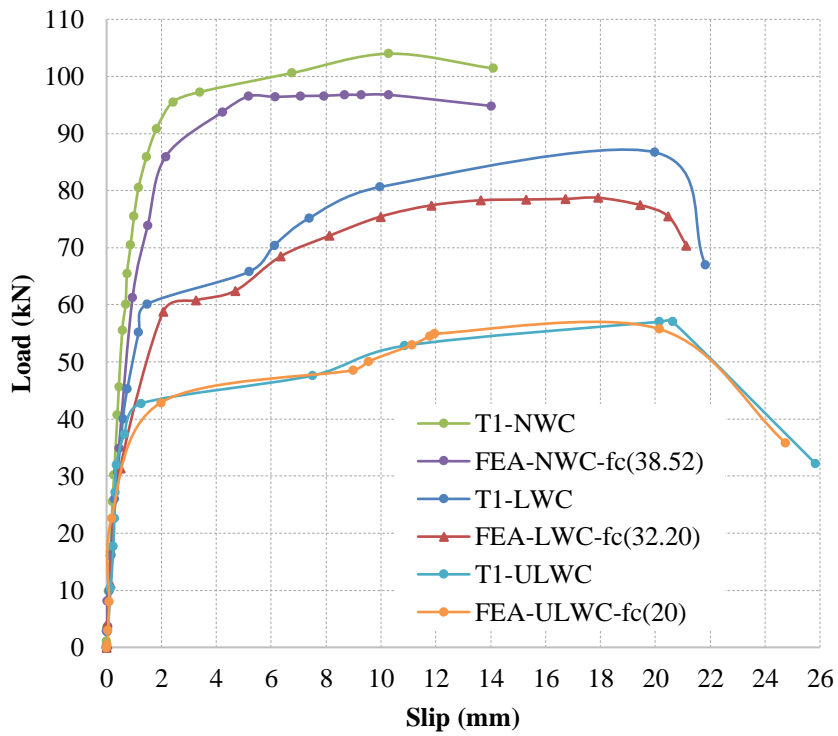
Fig. 21: Comparison of load-slip curves between FE models and push-out test specimens with WWSS
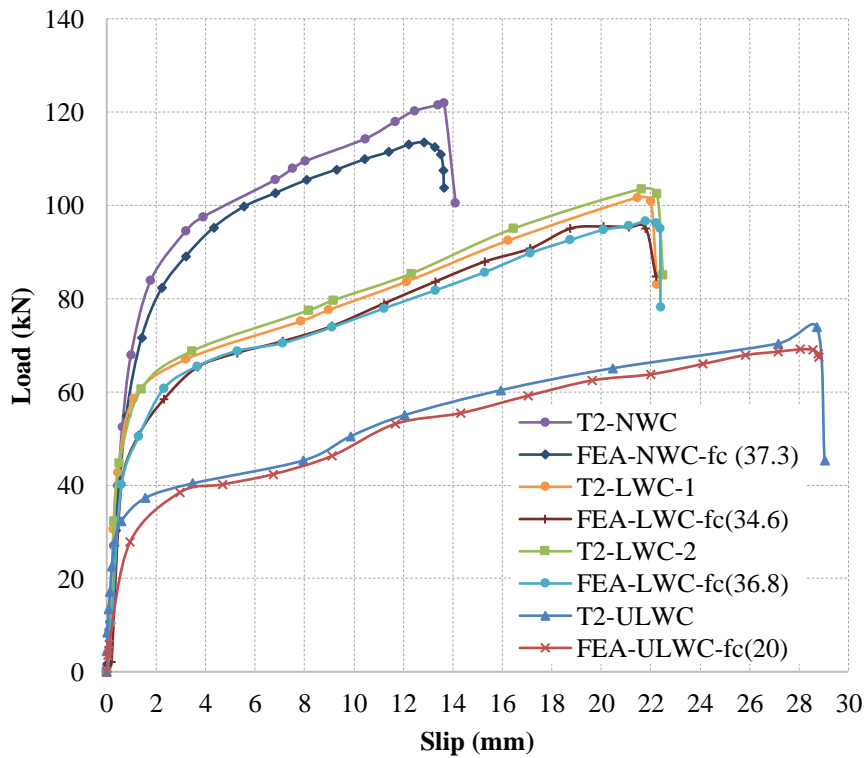
Fig. 22: Comparison of load-slip curves between FE models and push-out test specimens with WWSS with dowels

In Figs 23-28, stress contour plots of steel beam and concrete slab of FE models with WWSS or WWSS with dowels and different types of used concrete are illustrated and compared for the same group test with different types of used concrete. The stress plots clearly demonstrated the bending of WWSS and dowels and the cracking of the concrete in the shear direction when subjected to the longitudinal shear slip. Higher stresses (higher shear resistances) have been obtained from the FE models with higher concrete strength for both testing groups T1 and T2. In addition, using shear connection system of WWSS with dowels in the FEA study has led to higher stresses (higher shear resistances) when compared with the FE models with shear connection system of WWSS for the same type of concrete as shown in Figs 23-28, respectively. These results were consistent with the results obtained from the experimental work.

(a)   (b)
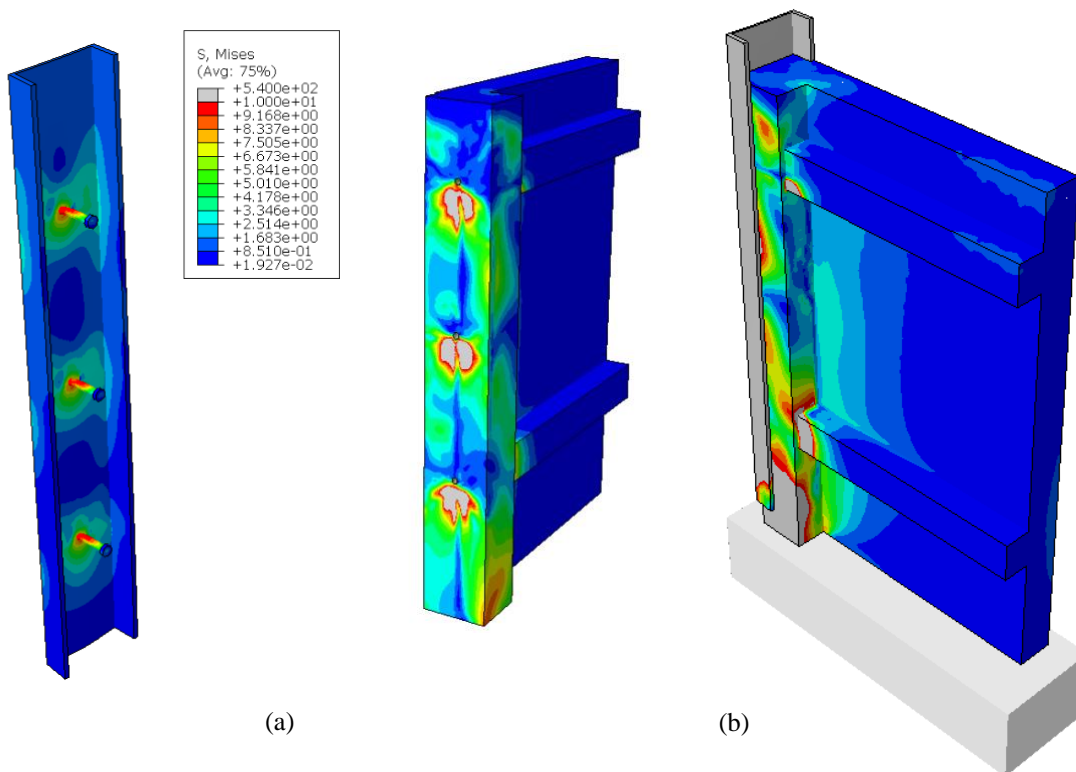
Fig. 23: Stress contour plots of (a) steel beam: (b) concrete slab of FEA model with WWSS and NWC-fc-38.52MPa

33

(a)

(b)
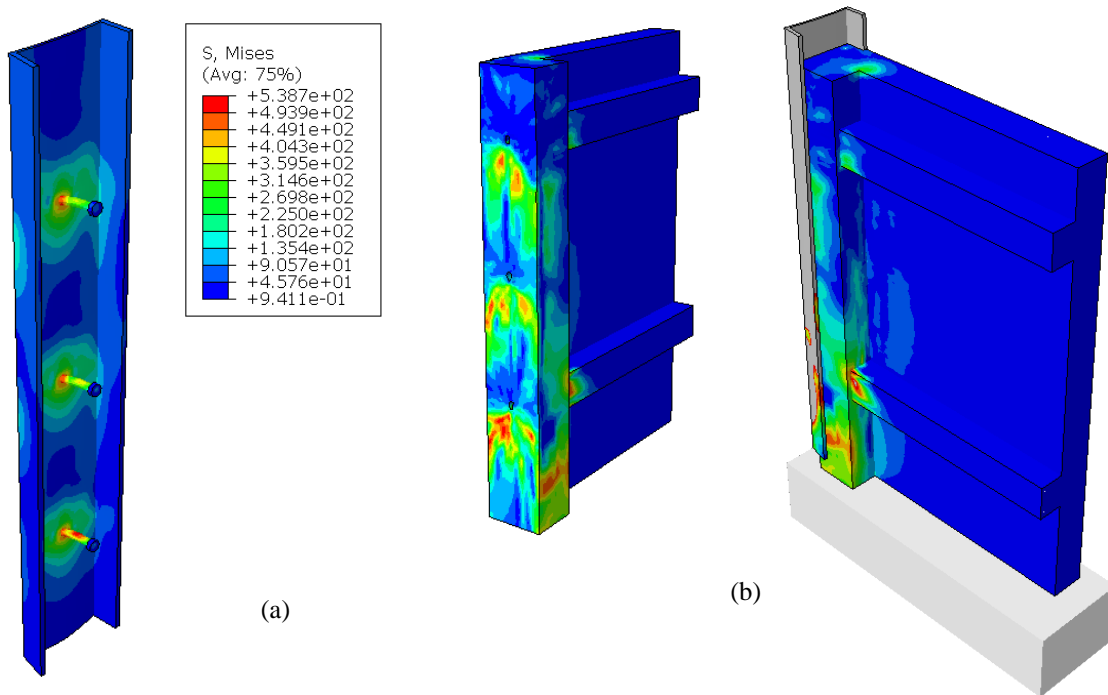
Fig. 24: Stress contour plots of (a) steel beam: (b) concrete slab of
FEA model with WWSS and LWC-fc-32.20MPa

(a)

(b)
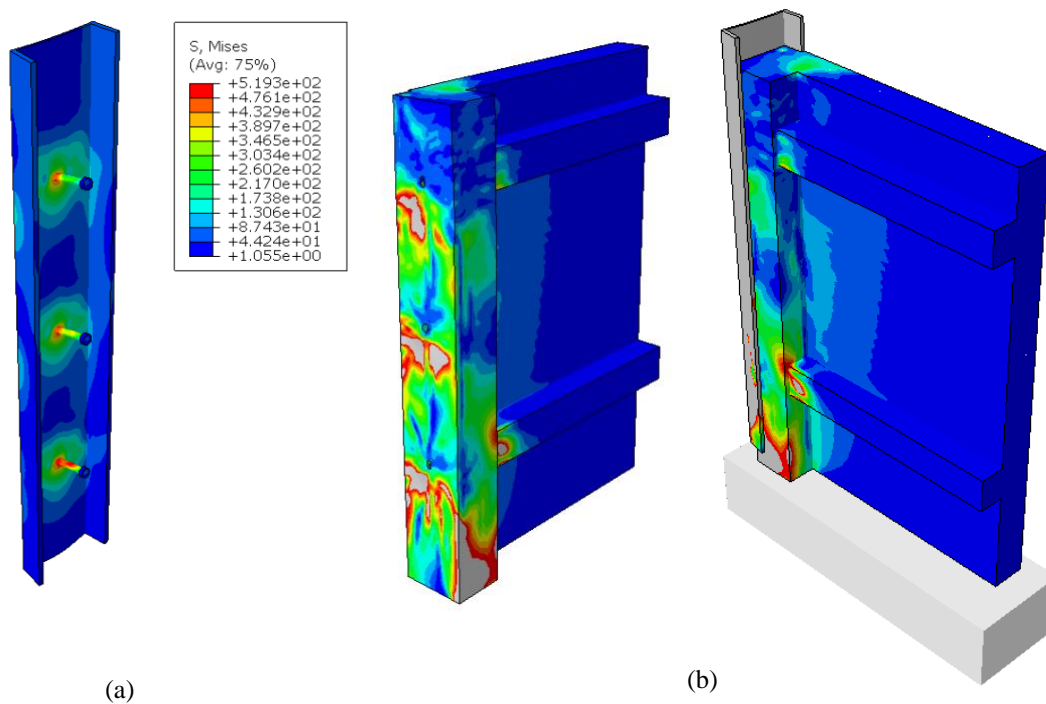
Fig. 25: Stress plots of (a) steel beam; (b) concrete slab of FEA model with
WWSS and ULWC-fc-20MPa

(a)

(b)
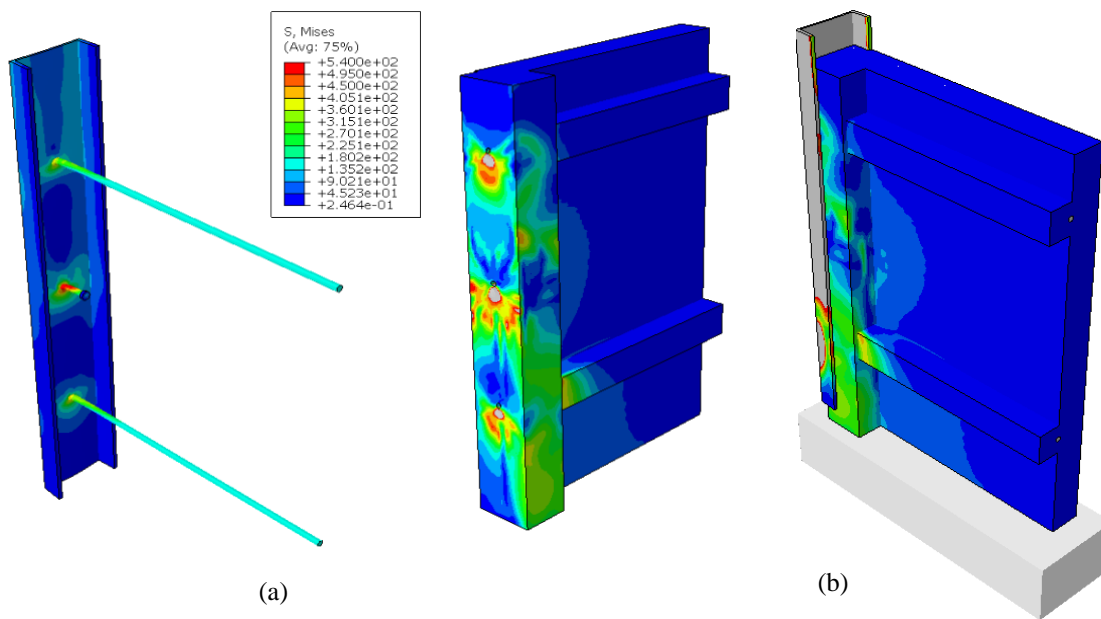
Fig. 26: Stress contour plots of (a) steel beam; (b) concrete slab of FEA
model with WWSS with dowels and NWC-fc-37.3MPa

(a)

(b)
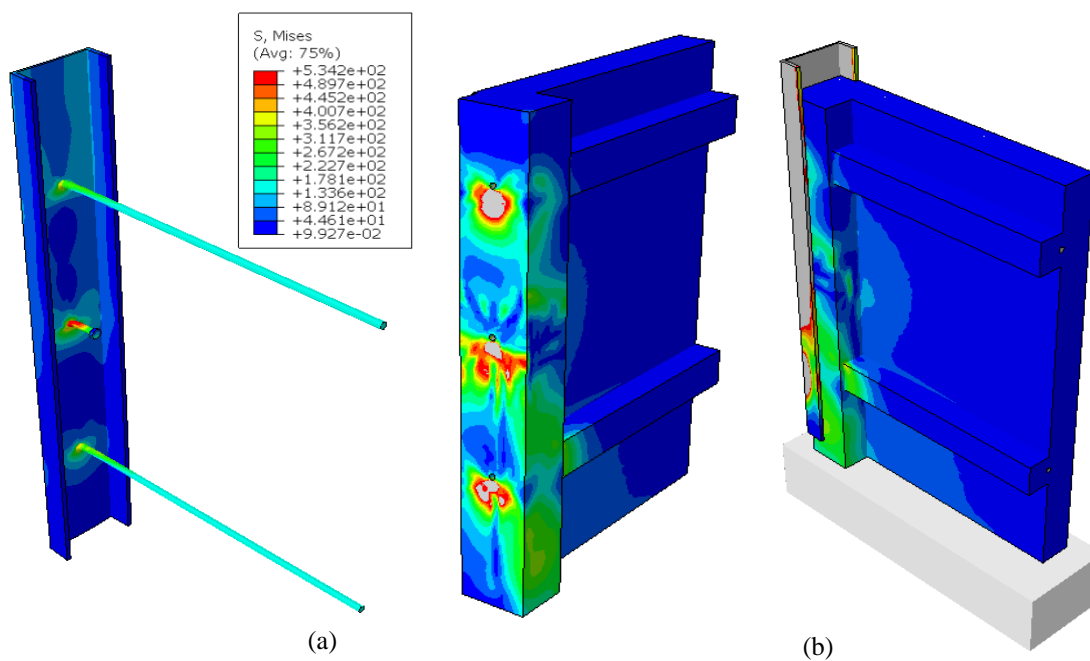
Fig. 27: Stress contour plots of (a) steel beam; (b) concrete slab of
FEA model with WWSS with dowels and LWC-fc-36.8MPa
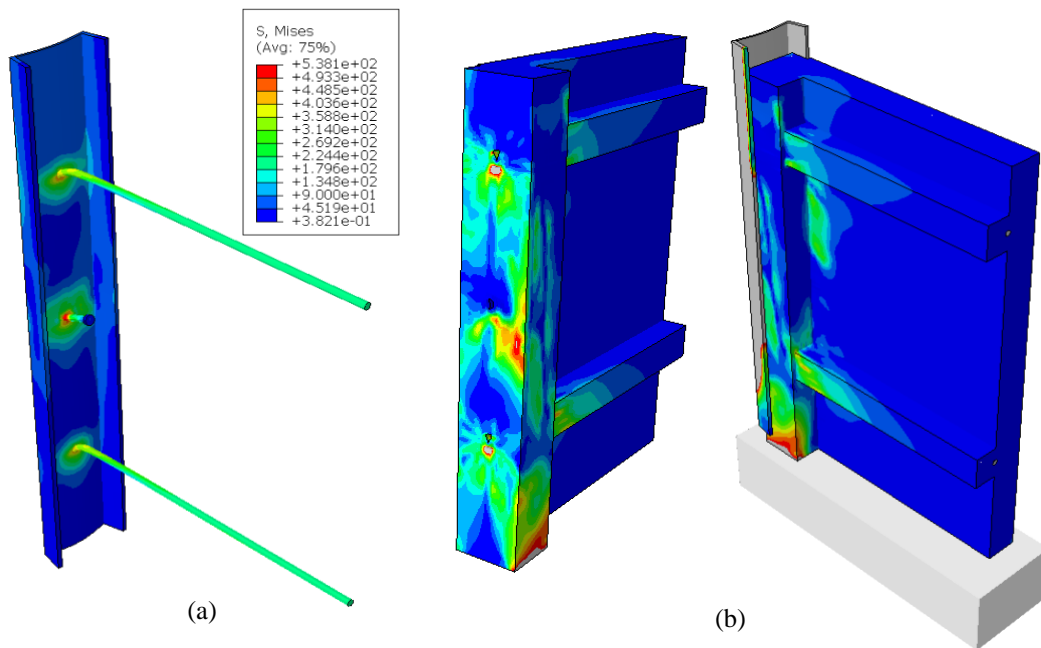
Fig. 28: Stress contour plots of (a) steel beam; (b) concrete slab of FEA model
with WWSS with dowels and ULWC-fc-20MPa

The contour plots of vertical displacement (slip) and cracks of the FEA for the models with
WWSS or WWSS with dowels and different types of used concrete are shown in Figs. 29-34,
respectively. Lower vertical displacements (lower slip capacity) have been observed form the
FE models with WWSS in contrast with FE models with WWSS with dowels which conducted
higher vertical displacements a shown in Figs 29-34. In addition, the FE models with higher
concrete strength have higher vertical displacement (higher slip capacity) than the FE models
with lower concrete strength for both testing groups T1 & T2. Good agreement has been shown
between the results of the FE models and the experimental work.
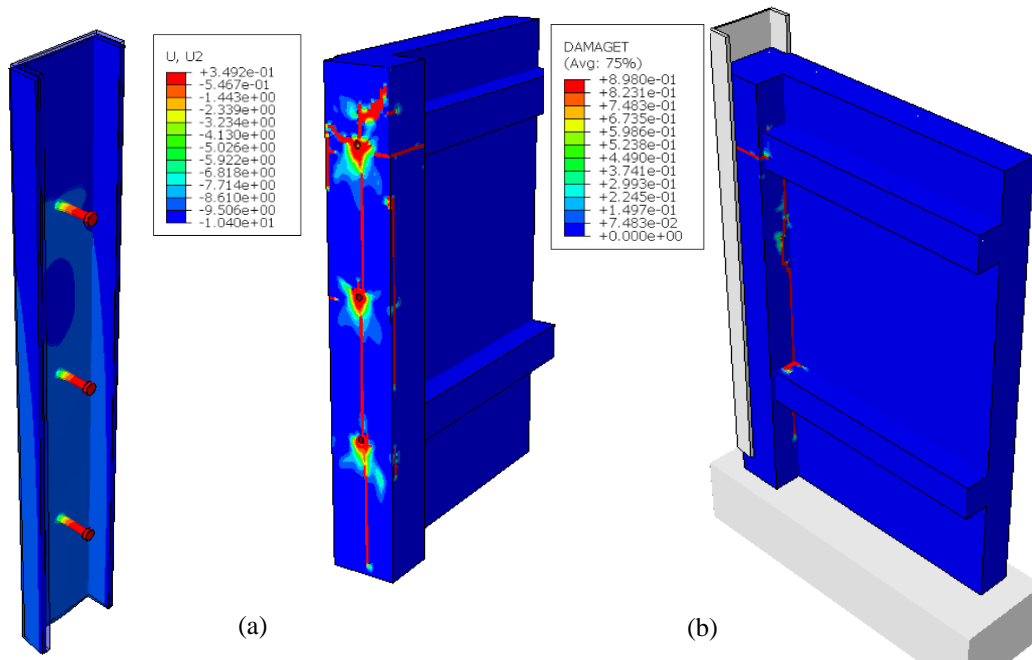
Fig. 29: Contour plots of: (a) vertical displacement (slips); (b) cracks
of FEA model with WWSS and NWC-fc-38.52MPa
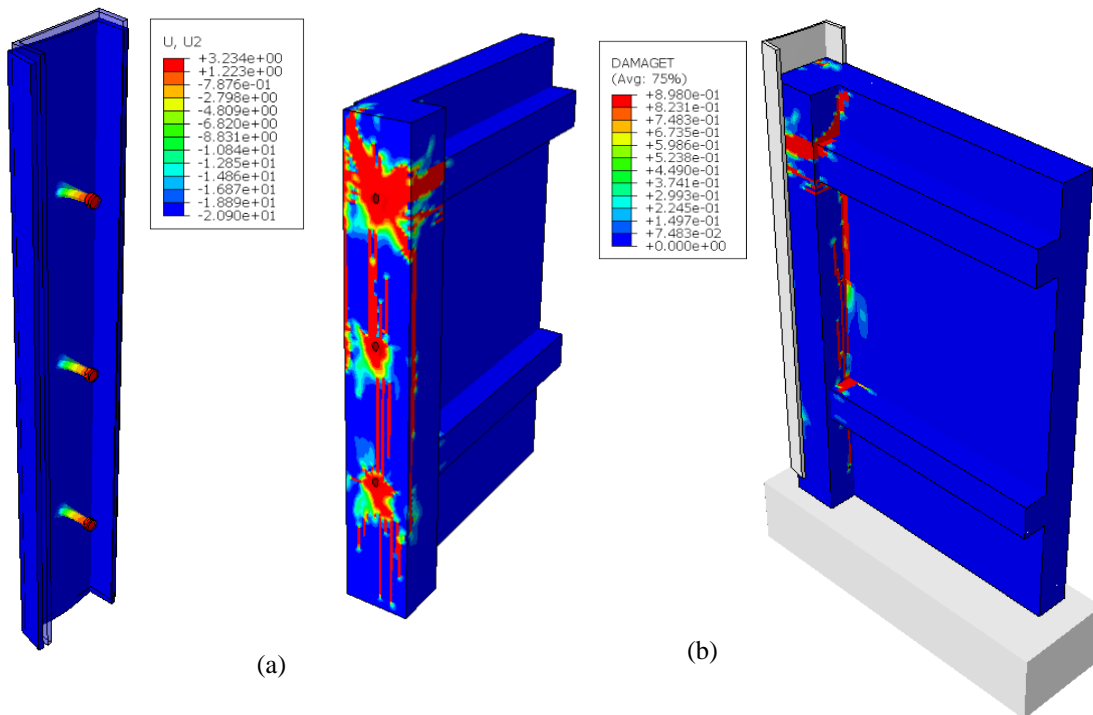
Fig. 30: Contour plots of: (a) vertical displacement (slips); (b) cracks
of FEA model with WWSS and LWC-fc-32.20MPa
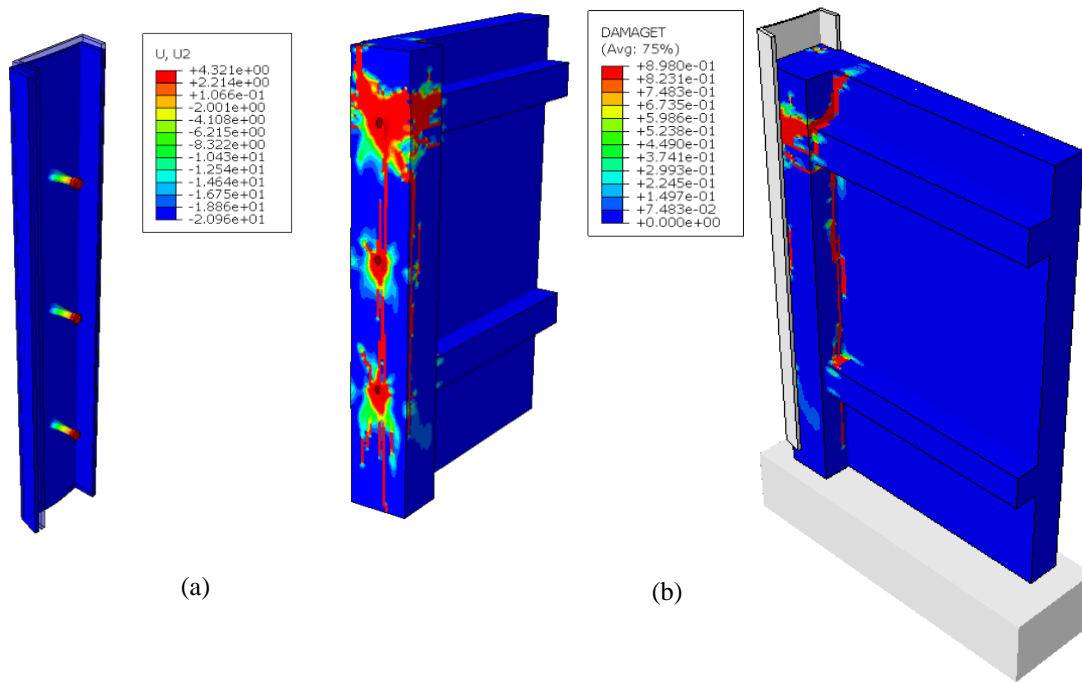
Fig. 31: Contour plots of: (a) vertical displacement (slips); (b) cracks
of FEA model with WWSS and ULWC-fc-20MPa
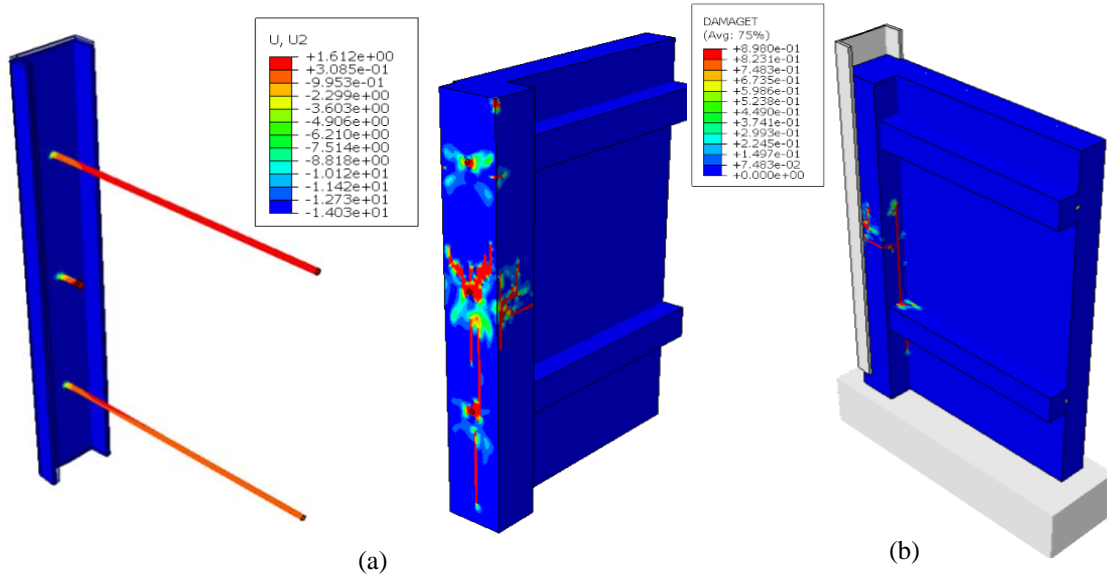
Fig. 32: Contour plots of: (a) vertical displacement (slips); (b) cracks
of FEA model with WWSS with dowels and NWC-fc-37.3MPa
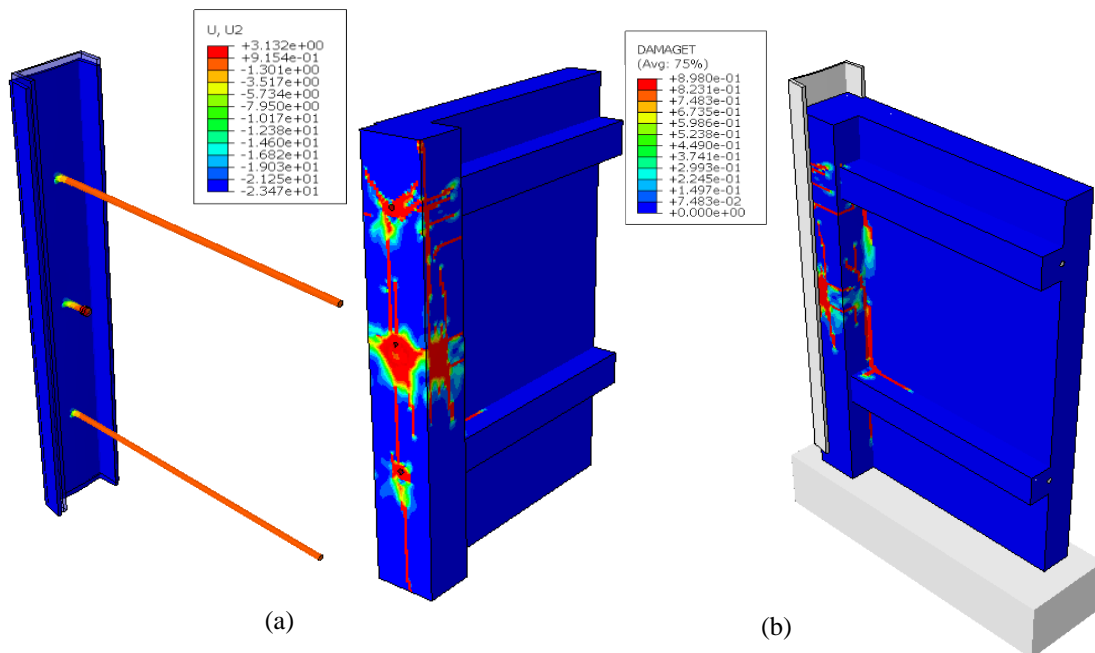
Fig. 33: Contour plots of: (a) vertical displacement (slips); (b) cracks
of FEA model with WWSS with dowels and LWC-fc-36.8MPa
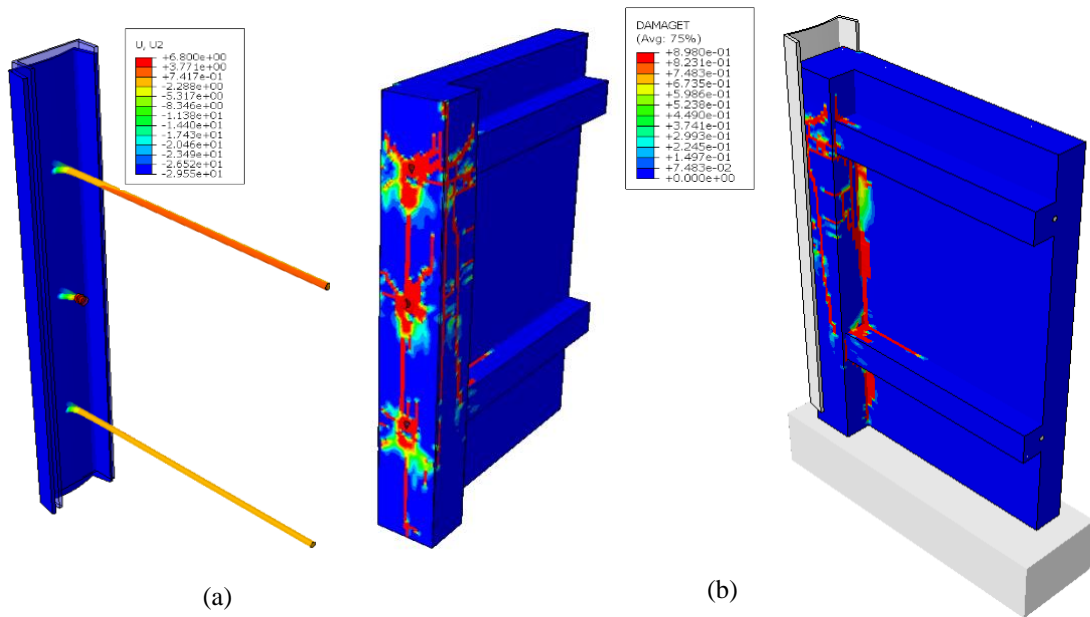
Fig. 34: Contour plots of: (a) vertical displacement (slips); (b) cracks
of FEA model with WWSS with dowels and ULWC-fc-20MPa

A comparison between the FE models' modes of failure of (steel beam, shear connection systems and concrete slabs) and the experimental work failure modes is illustrated in Figs.35 & 36. The failure modes of the FE models have excellent agreement with the failure modes of the experimental work specimens.

To conclude, the above validation has shown excellent agreement between the results of the FEA and the push-out tests, in the terms of the failure load, slip, stress results and failure mode. It was demonstrated that the FE model used for the validation is reliable and could be used to carry out a parametric study on the shear connection systems.

(a) T1-NWC

(b) T1-LWC

(c) T1-ULWC
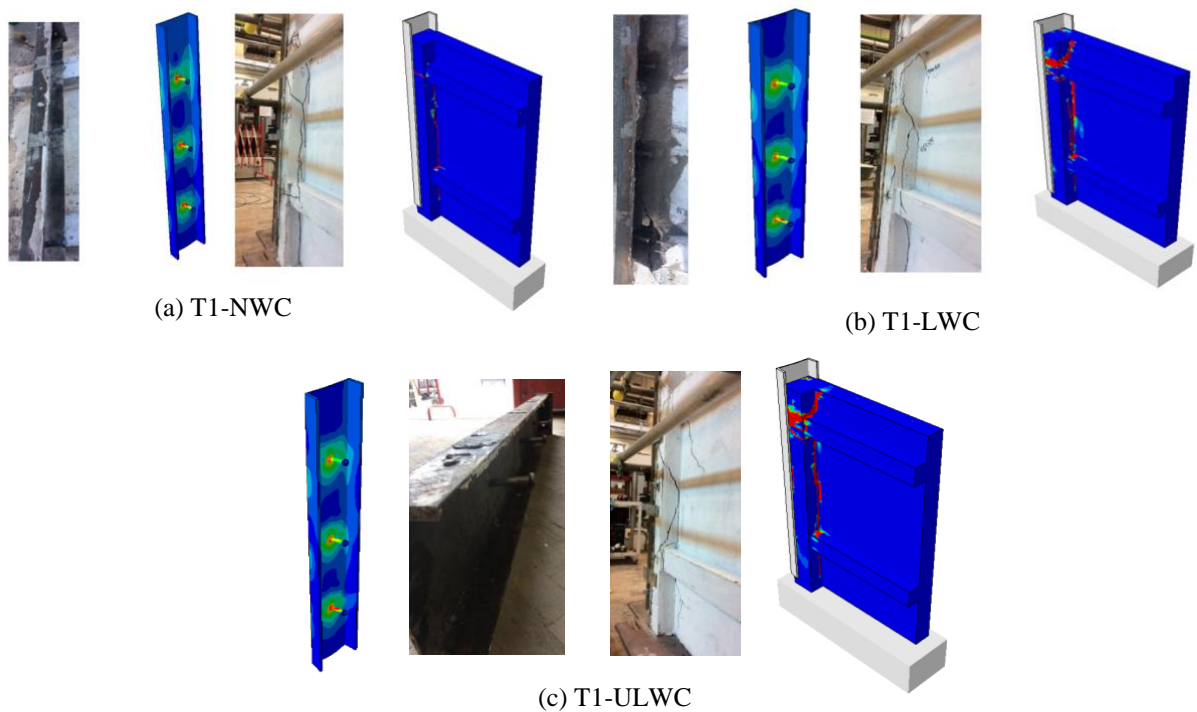
Fig. 35: Comparison of the shear stud connectors' failures and concrete slab failures between the FE models and T1specimens with WWSS

(a) T2-NWC   (b) T2-LWC

(c) T2-ULWC
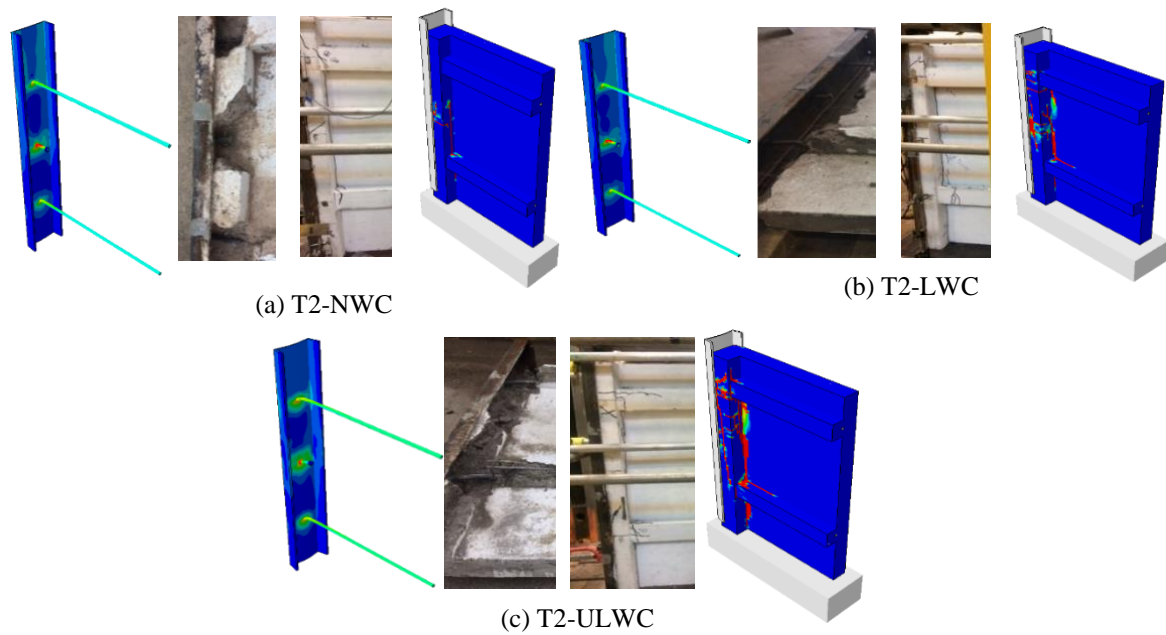
Fig. 36: Comparison of the shear stud connectors' failures and concrete slab failures between the FE models and T2 specimens with WWSS with dowels

4. PARAMETRIC STUDY

The elaborated FE model of the push-out test is used to carry out a parametric study. The variable parameters investigated in the FEA parametric study were the strengths for different types of concrete (NWC, LWC and ULWC) and the diameter of the shear connection systems (WWSS, WWSS with dowels). The concrete strength for all types of concrete varied between $20 N/mm^2$ to $35 N/mm^2$ and the connection system diameter varied between 16 mm, 19 mm, 20 mm and 22 mm, and the height of the shear studs between 75 mm and 100 mm.

The FE models for the push-out test with WWSS with diameters of 16 mm and 22 mm, heights of 75 mm and 100 mm, and WWSS with dowels with diameters of 16 mm and 22 mm were developed. These FE models contained the same types of elements, boundary conditions and contact model with that of the calibrated FE model, with 19 mm diameter for the WWSS and 20 mm with WWSS with dowels.

The results of the FE parametric study are summarised in Tables A-1 and A-2 in Appendix A. The load-slip curves of the FE models with WWSS dimensions of 16×75, 19×100 and 22×100 mm and with 16 mm, 20 mm and 22 mm dowels diameters are illustrated in Figs. B-1 to B-6

41

in Appendix B. These load-slip curves demonstrated that the FE models with the same diameter had different slip stiffness, where the failure loads and slips varied with the concrete strengths. The slip results were also compared for the FE models with different shear connection systems' dimensions at concrete strengths of 20, 30 and 35 N/mm^2, as shown in Figs. B-7 to B-12 in Appendix B. It was demonstrated that the slip stiffness of the shear connection systems is influenced by the diameters of the shear connection system, since the slip stiffness of the FE models increased with the increase of the diameter of the shear connection system. The FEA of the shear connection systems also demonstrated how the failure loads were dependent on the diameter of the shear connection system. For the shear connection system with the same concrete strength, the failure loads increased with an increase in the shear connection systems' diameters.

5. VERIFICATION OF SHEAR RESISTANCE CALCULATION WITH FEA RESULTS

The method for calculating the shear resistance of the connection systems (Eq. 16) in the companion paper [1] is represented by two terms: the compressive resistance of the concrete, and the tensile resistance of the steel elements, i.e., studs or dowels. The method of combining the compressive resistance of the concrete and tensile resistance of the steel elements to calculate the shear resistance of the shear connection systems is based on the failure mechanism as shown in the push-out tests. The results of the FEA parametric study were used to further verify the proposed formula (Eq. 16) in the companion paper [1] which obtained for calculating the shear resistance of the shear connection systems.

$$P_{sd} = 1.873(f_{ck}\, d\, a_r)^{0.835} \leq 0.8 f_u A_s \tag{16}$$

Where P_{sd} is the shear resistance of shear stud or dowel, f_{ck} is the cylinder compressive strength of concrete, d is the diameter of stud or dowel, and a_r is the distance from first stud or dowel to the top of concrete, f_u is the ultimate tensile strength of the material of the stud or dowel which should not be greater than 500 N/mm^2, and A_s is the cross-sectional area of the shear the stud or dowel

The FEA parametric study investigated both the shear connection systems with the concrete strengths that varied between 20 N/mm^2 to 35 N/mm^2, dowels diameters of 16 mm, 20 mm and 22 mm and studs of 16×75 mm, 19×100 mm and 22×100 mm. The results of the FEA were

compared with the calculated results using Eq.16 in the companion paper [1], which was the method obtained from the regression analysis.

The comparison showed that the calculated shear resistance of the shear connection systems using Eq. 16 in the companion paper [1] is (lower or higher) than that obtained in the FEA, as demonstrated in Tables A-3 to A-8 in Appendix A. The average ratios for the shear resistance of the calculation to FEA were 0.962, 1.108 and 1.08 for the WWSS with dimensions of 16×75 mm, 19×100m and 22×100 mm, respectively. In addition, the average ratios for the shear resistance of the calculation to FEA were 0.894, 0.954 and 0.901 for the WWSS with dowels with diameters of 16 mm, 20 mm and 22 mm, respectively.

6. CONCLUDING REMARKS

A finite element analysis study of the structural behaviour of the shear connection of prefabricated ultra-lightweight concrete slab was presented. The FE models were developed based on the push-out test specimens and including nonlinear contact modelling considering the longitudinal interface slip, the friction between the concrete slab, shear connectors and steel beams. The FE models were calibrated and validated against 8 test results in the companion paper [1], and were then used to perform intensive 84 parametric studies. The following conclusions are drawn:

1. The FE models have proven the capability to accurately and reliably simulate the overall behaviour of the prefabricated ultra-shallow flooring system subjected to longitudinal shear slip.

2. The prefabricated ultra-shallow flooring system has demonstrated an increase in the shear resistance of the shear connection systems, with an increase in concrete strength for the different types of concrete.

3. The shear resistance of the shear connection systems increases with an increase in the WWSS diameter, along with height and dowel diameters, due to the increase of the shear interaction area, as well as the concrete bearing area.

4. The calculated results using Eq. 16 in the companion paper [1] were very close to the results of the FEA parametric study, given that the average ratios of the calculated shear resistance to results of the FEA were 0.962, 1.108 and 1.08 for the WWSS with dimensions of 16×75 mm,

19×100 mm and 22×100 mm, respectively and 0.894, 0.954 and 0.901 for the WWSS with dowels with diameters of 16 mm, 20 mm and 22 mm, respectively.

5. The shear resistance of the shear connection systems obtained from the calculation method, Eq. 16 [1], were very close to the results of the push-out tests.

7. ACKNOLWGEMENTS

8. REFERENCES

[1] I.M. Ahmed, and K.D. Tsavdaridis, 2020. Shear connection of prefabricated slabs with LWC-Part1: Experimental and analytical studies. Journal of Constructional Steel Research, 169, p.106016.

[2] I.M. Ahmed, and K.D. Tsavdaridis, A new breed of sustainable ultra-lightweight and ultra-shallow steel-concrete composite flooring system: LCA, Proceedings. Postgraduate Research Conference, Faculty of Engineering, 30–31 Mar 2017, The University of Leeds, Leeds, UK, 2017.

[3] I.M. Ahmed, K.D. Tsavdaridis, and F. Neysari, A New Breed of Sustainable Ultra-Lightweight and Ultra-Shallow Steel-Concrete Composite Flooring System: life Cycle Assessment of Materials. CESARE'17 International Conference of Coordinating Engineering for Sustainability and Resilience, Dead Sea, Jordan 3-8 May 2017, 2017.

[4] I.M. Ahmed, K.D. Tsavdaridis, and F. Neysari, Push-out shear tests for a novel pre-fabricated shallow steel-concrete composite flooring system, The 12th International Conference on Advances in Steel-Concrete Composite Structures (ASCCS 2018). 27–29 June 2018, Valencia, Spain, 2018.

[5] I.M. Ahmed, and K.D. Tsavdaridis, Life cycle assessment (LCA) and cost (LCC) studies of lightweight composite flooring systems, Journal of Building Engineering 20 (2018) 624–633.

[6] I.M. Ahmed, and K.D. Tsavdaridis, The evolution of composite flooring systems: and applications, testing. Modelling and Eurocode design approaches, Journal of Constructional Steel Research. 155 (2019) 286–300.

[7] K.D. Tsavdaridis, C. D'Mello, and M. Hawes, Experimental study of ultra-shallow floor beams (USFB) with perforated steel sections, The 11th Nordic Steel Construction Conference 2009 (NSCC 2009). 2-4 September 2009, Malmö, Sweden, Reference no: 128 2009, pp. 312–319.

[8] K.D. Tsavdaridis, C. D'Mello, and B.Y. Huo, Computational study modelling the experimental work conducted on the shear capacity of perforated Concrete-Steel Ultra Shallow Floor beams (USFB), The 16th National Concrete Conference. 21-23 October 2009, Paphos, Cyprus, Reference no: 201101 2009, p. 159.

[9] K.D. Tsavdaridis, Structural Performance of Perforated Steel Beams with Novel Web Openings and with Partial Concrete Encasement, Doctoral Thesis City University, London, 2010.

[10] K.D. Tsavdaridis, and A. Giaralis, Derivation of dynamic properties of steel perforated ultra-shallow floor beams (USFB) via finite element modal analysis and experimental verification, The 7th Greek National Steel Structures Conference. 28 September – 1 October 2011, Volos, Greece, Reference no: 053, Vol. 2 2011, pp. 321–329.

[11] K.D. Tsavdaridis, C. D'Mello, and B.Y. Huo, Experimental and Computational Study of vertical shear behaviour of partially encased perforated steel beams, Engineering Structures. 56 (2013) 805–822.

[12] B. Yu Huo, C. D'Mello, and K.D. Tsavdaridis, Experimental and analytical study of pushout shear tests in ultra-shallow floor beams, The 34th International Association for Bridge and Structural Engineering Symposium (IABSE 2010). 22–24 September 2010, Venice, Italy, IABSE Proceedings 2010, pp. 31–38.

[13] M. Veljkovic, Behaviour and resistance of composite slabs, PhD Thesis, Lulea University of Technology, Lulea, Sweden, 1996.

[14] R. Abdullah, and WS. Easterling, Determination of composite slab strength using a new elemental test method. Journal of Structural Engineering, ASCE 2007; 133(9):1268–77

[15] BJ. Daniels, and M. Crisinel, Composite slab behaviour and strength analysis. Part I: calculation procedure. Journal of Structural Engineering, ASCE 1993; 119(1):16–35.

[16] BR. Widjaja, Analysis and design of steel deck–concrete composite slabs, PhD Thesis, USA: Virginia Polytechnic Institute and State University, 1997.

[17] T. Tsalkatidis, and A. Avdelas, The unilateral contact problem in composite slabs: experimental study and numerical treatment. Journal of Constructional Steel Research 2010; 66(3):480–6.

[18] M. Ferrer, and F. Marimon, FEM modelling of composite slabs' shear connection and new friction system based on steel sheet punching, steel concrete composite and hybrid structures. In: Lam Dennis, editor. Proceeding of the 9th International Conference on Steel Concrete Composite and Hybrid Structures. Research Publishing Services; 2009.

[19] ABAQUS, Theory Manual, Ver 6.14, Dassault Systèmes Simula Corp, 2014 (Providence, RI, USA).

[20] H.T. Nguyen, and S.E. Kim, 2009. Finite element modelling of push-out tests for large stud shear connectors. Journal of Constructional Steel Research, 65(10-11), pp.1909-1920.

[21] D. Jung, 1998. Study of dynamic explicit analysis in sheet metal forming processes using faster punch velocity and mass scaling scheme. Journal of materials engineering and performance, 7, 479-490.

[22] W. Algaard, J. Lyle, and C. Izatt, 2005, May. Perforation of composite floors. In 5th European LS-DYNA users conference (pp. 1123-1130).

[23] M.Q. Nguyen, D.J. Elder, J. Bayandor, R.S. Thomson, and M.L. Scott, 2005. A review of explicit finite element software for composite impact analysis. Journal of Composite Materials, 39(4), pp.375-386.

[24] EN 1992-1-1 2004. Eurocode 2: Design of concrete structures: Part 1-1: General rules and rules for buildings. London: British Standards Institution.

[25] B.I. Karlsson, and E.P. Sorensen, (2006a) ABAQUS: Analysis user's manual version6.5, Pawtucket, Rhode Island, Hibbitt Publication.

[26] A. Hillerborg, 1985. The theoretical basis of a method to determine the fracture energy of concrete. Materials and structures, 18(4), pp.291-296.

[27] H.A.W. Cornelissen, D.A. Hordijk, and H.W. Reinhardt, 1986. Experimental determination of crack softening characteristics of normal weight and lightweight. Heron, 31, p.45.

[28] T.H. Almusallam, and S.H. Alsayed, 1995. Stress-strain relationship of normal, high-strength and lightweight concrete. Magazine of Concrete Research, 47(170).

[29] ISO 6892-1:2009 Metallic materials – tensile testing – Part 1: Method of test at room temperature.

[30] C. Xu, K. Sugiura, C. Wu, and Q. Su, 2012. Parametrical static analysis on group studs with typical push-out tests. Journal of constructional steel research, 72, pp.84-96.

[31] J. Qureshi, D. Lam, and J. Ye, 2010. Finite element modelling of shear connection behaviour in a push test using profiled sheeting. Advances and Trends in Structural Engineering, Mechanics and Computation, p.167.

[32] ABAQUS Documentation, version 6.8.1. Dassault system, USA; 2008.

[33] E. Ellobody, B. Young, and D. Lam, 2006. Behaviour of normal and high strength concrete-filled compact steel tube circular stub columns. Journal of Constructional Steel Research, 62(7), pp.706-715.

[34] B.I. Karlsson, and E.P. Sorensen, (2006b) ABAQUS: Analysis user's manual volume IV: Element, Pawtucket, Rhode Island, Hibbitt Publication.

[35] EN1994-1-1: 2004: Eurocode 4. Design of Composite Steel and Concrete Structures, Part 1-1: General Rules and Rules for Buildings.

APPENDIX A

Table A-1: Results of the failure loads and slips of the FEA parametric study of web-welded shear stud connection system (WWSS)

Shear Connection Type	Concrete Type	Concrete Strength		E_c (MPa)	Failure Load (kN) of the FEA Model			Ultimate Slip (mm) of the FEA Model		
		f_c (MPa)	f_t (MPa)		16×75mm	19×100mm	22×100mm	16×75mm	19×100mm	22×100mm
WWSS	NWC	20	2.12	28608	71.85	84.15	93.47	15.47	8.15	20.95
WWSS	NWC	25	2.45	29962	75.45	87.4	97.45	14.58	8.78	18.69
WWSS	NWC	30	2.56	31187	78.25	90.58	101.85	13.45	9.27	17.24
WWSS	NWC	35	2.78	32308	81.65	93.85	105.42	12.45	10.45	16.78
WWSS	NWC	38.52	2.88	33047	82.36	96.78	108.23	11.21	9.27	15.85
WWSS	LWC	20	1.45	17183	61.68	68.65	78.69	19.47	17.86	21.95
WWSS	LWC	25	1.52	17996	64.65	72.85	82.12	18.36	18.47	19.62
WWSS	LWC	30	1.83	18731	67.85	75.85	85.45	17.45	19.14	17.48
WWSS	LWC	32.32	1.61	31719	69.65	78.75	88.74	15.14	17.90	16.80
WWSS	LWC	35	2.11	19405	71.47	80.24	90.34	14.75	16.85	15.47
WWSS	ULWC	20	1.36	9989	47.65	55.74	68.23	13.96	20.15	11.96
WWSS	ULWC	25	1.42	10461	50.48	58.96	71.85	15.28	19.78	13.14
WWSS	ULWC	30	1.70	10889	53.94	61.78	74.65	16.37	17.86	15.78
WWSS	ULWC	35	1.98	11281	56.98	63.45	77.58	19.55	15.96	17.95

Table A-2: Results of the failure loads and slips of the FEA parametric study of web-welded shear stud with dowels (WWSS with dowels)

Shear Connection Type	Concrete Type	Concrete Strength		E_c (MPa)	Failure Load (kN) of the FEA Model			Ultimate Slip (mm) of the FEA Model		
		f_c (MPa)	f_t (MPa)		d 16mm	d 20mm	d 22mm	d 16mm	d 20mm	d 22mm
WWSS with dowels	NWC	20	2.12	28608	84.95	100.12	114.26	13.78	14.52	22.45
WWSS with dowels	NWC	25	2.45	29962	87.56	103.87	118.78	12.45	13.45	20.45
WWSS with dowels	NWC	30	2.88	31187	93.74	106.98	121.85	11.65	12.26	18.96
WWSS with dowels	NWC	35	3.2	32308	96.45	110.72	125.85	10.98	11.44	16.87
WWSS with dowels	NWC	37.3	3.34	31937	97.63	113.54	127.66	10.04	12.84	15.64
WWSS with dowels	LWC	20	1.45	17183	68.86	84.32	98.78	24.95	25.78	31.45
WWSS with dowels	LWC	25	1.52	17996	72.95	87.69	102.47	22.78	24.56	28.95
WWSS with dowels	LWC	30	1.83	18731	76.12	90.85	105.96	19.78	23.45	27.95
WWSS with dowels	LWC	35	2.11	19405	79.78	93.12	108.23	18.85	22.65	26.78
WWSS with dowels	LWC	36.8	2.12	19635	82.78	96.62	110.45	17.42	21.79	25.78
WWSS with dowels	ULWC	20	1.38	9989	55.84	69.12	83.73	24.16	28.04	28.98
WWSS with dowels	ULWC	25	1.42	10461	58.96	74.01	86.18	23.17	25.78	25.12
WWSS with dowels	ULWC	30	1.70	10889	61.98	79.12	89.47	21.35	24.56	22.78
WWSS with dowels	ULWC	35	1.98	11281	64.45	85.78	92.78	19.95	23.65	20.17

Table A-3: Comparison between results of calculation and FEA for WWSS
of 16×75mm with d (19mm), ar (217.5mm), fu(455.5N/mm^2) and As (283.52mm^2)

	Concrete type	f_{ck} (N/mm^2)	$P_{sd}{}^*$ (kN)	FEA (kN)	Ratio Cal/FEA
WWSS with 19*100mm	NWC	16	62.01	84.15	0.736
	NWC	20	74.71	87.4	0.854
	NWC	24	87.00	90.58	0.960
	NWC	28	98.95	93.85	1.054
	NWC	30.81	107.20	96.78	1.107
	LWC	16	62.01	68.65	0.903
	LWC	20	74.71	72.85	1.025
	LWC	24	87.00	75.85	1.147
	LWC	25.85	98.95	78.75	1.256
	LWC	28	92.59	55.74	1.661
	ULWC	16	62.01	58.96	1.051
	ULWC	20	74.71	61.78	1.209
	ULWC	24	87.00	63.45	1.371
	ULWC	28	98.95	84.15	1.175
* calculated using Eq.16				Average	1.108

Table A-4 Comparison between results of calculation and FEA for WWSS of 19×100mm
with d (16mm), ar (217.5mm), fu(510N/mm^2) and As (201.06mm^2)

	Concrete type	f_{ck} (N/mm^2)	P$_{sd}$* (kN)	FEA (kN)	Ratio Cal/FEA
WWSS with 16*75mm	NWC	16	53.72	84.15	0.638
	NWC	20	64.73	87.4	0.74
	NWC	24	75.37	90.58	0.832
	NWC	28	85.73	93.85	0.913
	NWC	30.81	92.87	96.78	0.959
	LWC	16	53.72	68.65	0.782
	LWC	20	64.73	72.85	0.888
	LWC	24	75.37	75.85	0.993
	LWC	25.85	85.73	78.75	1.088
	LWC	28	80.21	80.24	0.999
	ULWC	16	53.72	55.74	0.963
	ULWC	20	64.73	58.96	1.097
	ULWC	24	75.37	61.78	1.219
	ULWC	28	85.73	63.45	1.351
* calculated using Eq. 16				Average	0.962

Table A-5: Comparison between results of calculation and FEA for WWSS of 22×100mm with d (22mm), ar (217.5mm), fu(500N/mm^2) and As (380.12mm^2

	Concrete type	f_{ck} (N/mm^2)	P_{sd}* (kN)	FEA (kN)	Ratio Cal/FEA
WWSS with 22*100mm	NWC	16	70.09	93.47	0.749
	NWC	20	84.44	97.45	0.866
	NWC	24	98.33	101.85	0.965
	NWC	28	111.84	105.42	1.06
	NWC	30.81	121.16	108.23	1.119
	LWC	16	70.09	78.69	0.89
	LWC	20	84.44	82.12	1.028
	LWC	24	98.33	85.45	1.15
	LWC	25.85	111.84	88.74	1.26
	LWC	28	104.64	90.34	1.158
	ULWC	16	70.09	68.23	1.027
	ULWC	20	84.44	71.85	1.175
	ULWC	24	98.33	74.65	1.317
	ULWC	28	111.84	77.58	1.441
* calculated using Eq. 16				Average	1.086

Table A-6: Comparison between results of calculation and FEA for WWSS with dowels of 16mm diameter with d (16mm), ar (217.5mm), fu(400N/mm^2) and As (201.06mm^2)

	Concrete type	f_{ck} (N/mm^2)	P_{sd}^* (kN)	FEA (kN)	Ratio Cal/FEA
Dowels with 16mm diameter	NWC	16	53.72	84.95	0.632
	NWC	20	64.73	87.56	0.739
	NWC	24	75.37	93.74	0.804
	NWC	28	85.73	96.45	0.888
	NWC	29.84	90.40	97.63	0.925
	LWC	16	53.72	68.86	0.780
	LWC	20	64.73	72.95	0.887
	LWC	24	75.37	76.12	0.990
	LWC	28	85.73	79.78	1.074
	LWC	29.44	89.39	82.78	1.079
	ULWC	16	53.72	55.84	0.962
	ULWC	20	64.73	58.96	1.097
	ULWC	24	75.37	61.98	1.216
	ULWC	28	85.73	64.45	1.330
* calculated using Eq. 16				Average	0.894

Table A-7: Comparison between results of calculation and FEA for WWSS with dowels of 20mm diameter with d (20mm), ar (217.5mm), fu(455.5N/mm^2) and As (314.15mm^2)

	Concrete type	f_{ck} (N/mm^2)	P_{sd}* (kN)	FEA (kN)	Ratio Cal/FEA
Dowels with 20mm diameter	NWC	16	64.73	100.12	0.646
	NWC	20	77.98	103.87	0.750
	NWC	24	90.81	106.98	0.848
	NWC	28	103.28	110.72	0.932
	NWC	29.84	108.92	113.54	0.959
	LWC	16	64.73	84.32	0.767
	LWC	20	77.98	87.69	0.889
	LWC	24	90.81	90.85	0.999
	LWC	28	103.28	93.12	1.109
	LWC	29.44	107.70	96.62	1.114
	ULWC	16	64.731	69.12	0.936
	ULWC	20	77.989	74.01	1.053
	ULWC	24	90.813	79.12	1.147
	ULWC	28	103.28	85.78	1.204
* calculated using Eq. 16				Average	0.954

8

Table A-8: Comparison between results of calculation and FEA for WWSS with dowels of 22mm diameter with d (22mm), ar (217.5mm), fu(500N/mm^2) and As (380.13mm^2)

	Concrete type	f_{ck} (N/mm^2)	P_{sd}* (kN)	FEA (kN)	Ratio Cal/FEA
Dowels with 22mm diameter	NWC	16	70.09	114.26	0.6134
	NWC	20	84.44	118.78	0.710
	NWC	24	98.33	121.85	0.806
	NWC	28	111.84	125.85	0.888
	NWC	29.84	117.94	127.66	0.923
	LWC	16	70.09	98.78	0.709
	LWC	20	84.44	102.47	0.824
	LWC	24	98.33	105.96	0.9272
	LWC	28	111.84	108.23	1.033
	LWC	29.44	116.62	110.45	1.055
	ULWC	16	70.09	83.73	0.837
	ULWC	20	84.44	86.18	0.979
	ULWC	24	98.33	89.47	1.099
	ULWC	28	111.84	92.78	1.205
* calculated using Eq. 16				Average	0.901

APPENDIX B

(a)

(b)

(c)
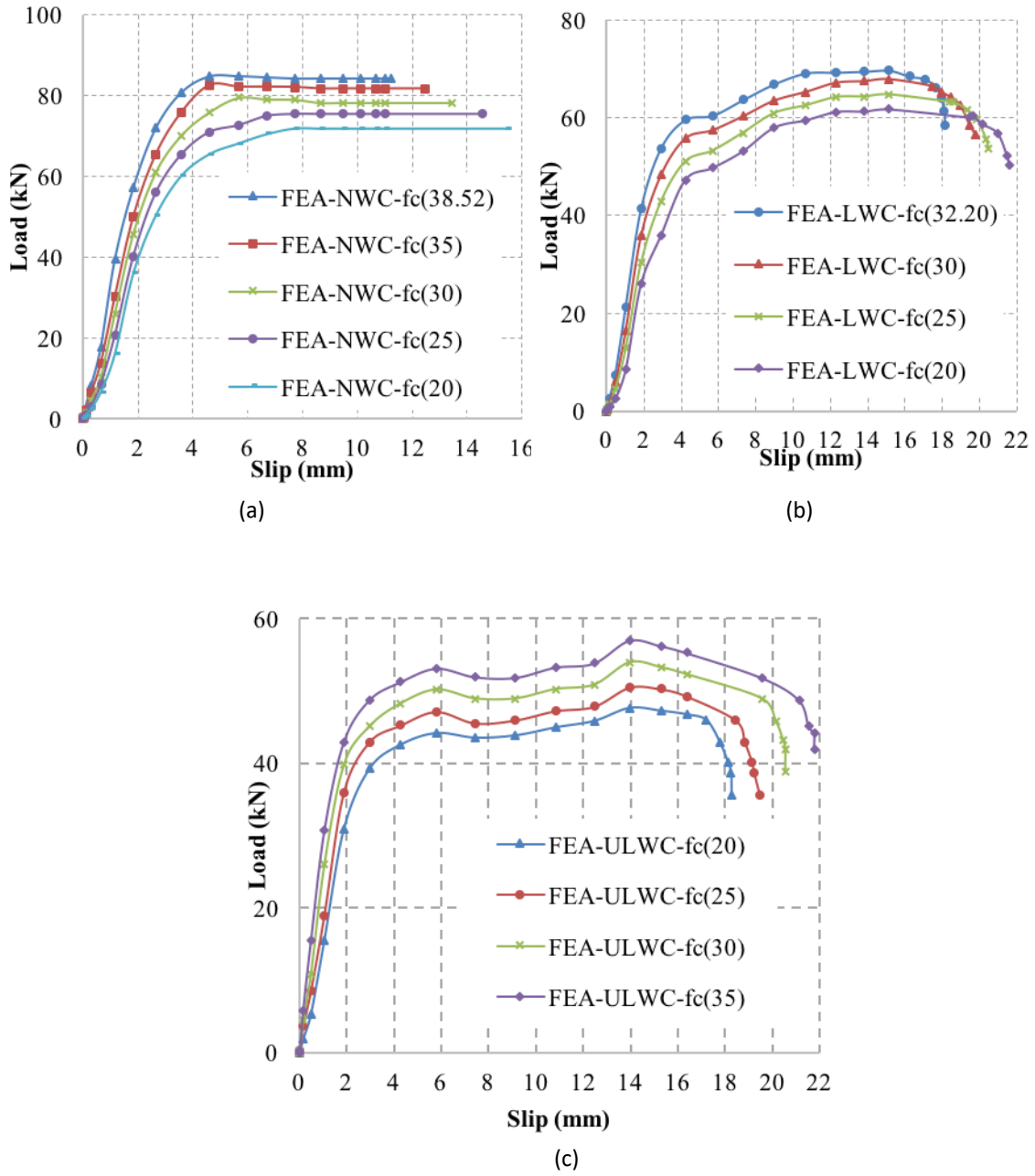
Fig. B-1: Load-slip curves of the FEA with WWSS 16×75mm
with different concrete types
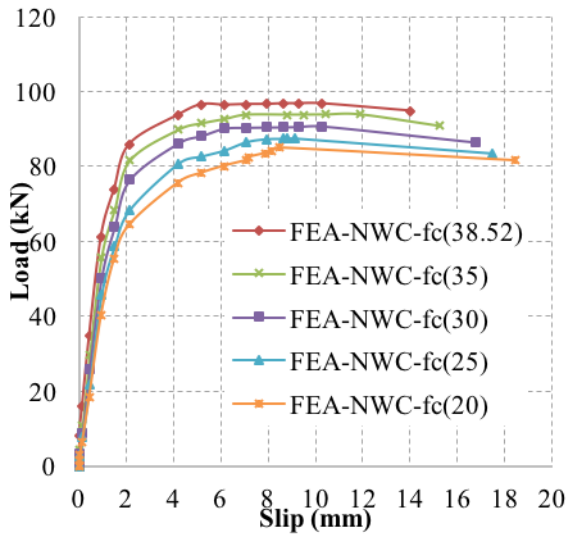
(a)
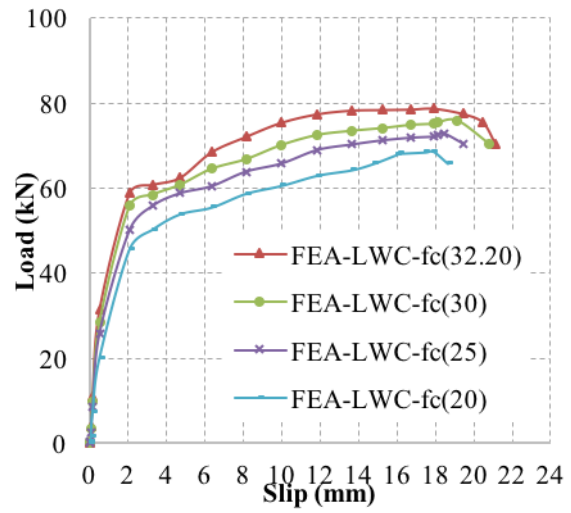
(b)
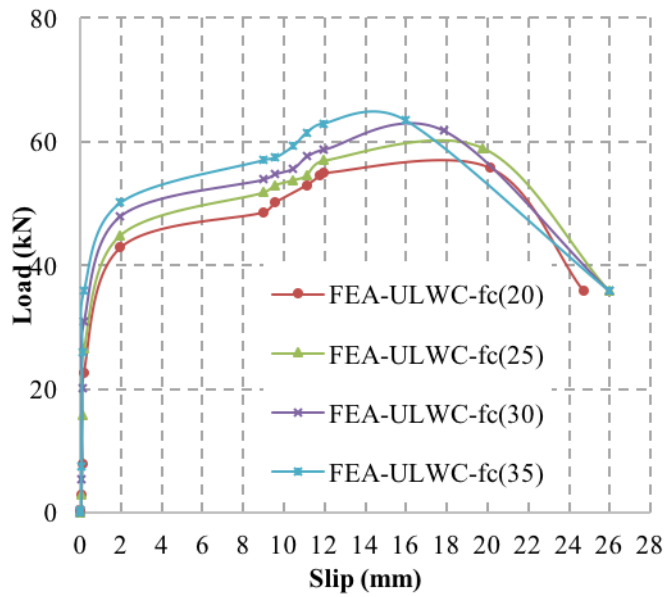
(c)

Fig. B-2: Load-slip curves of the FEA with WWSS 19×100mm
with different concrete types

(a)

(b)

(c)
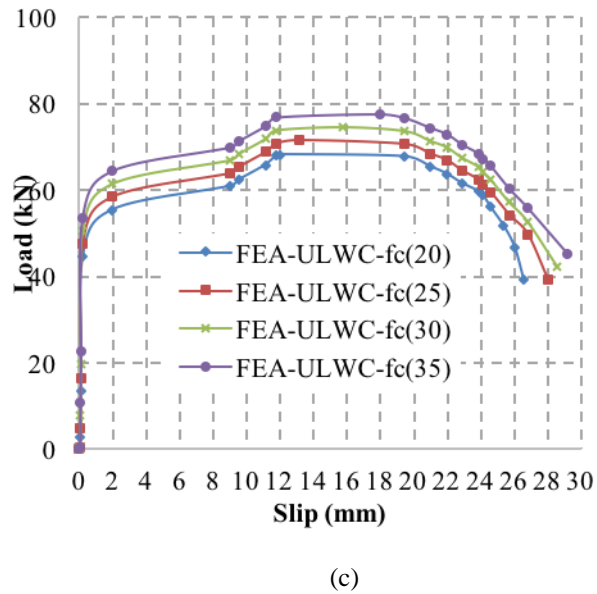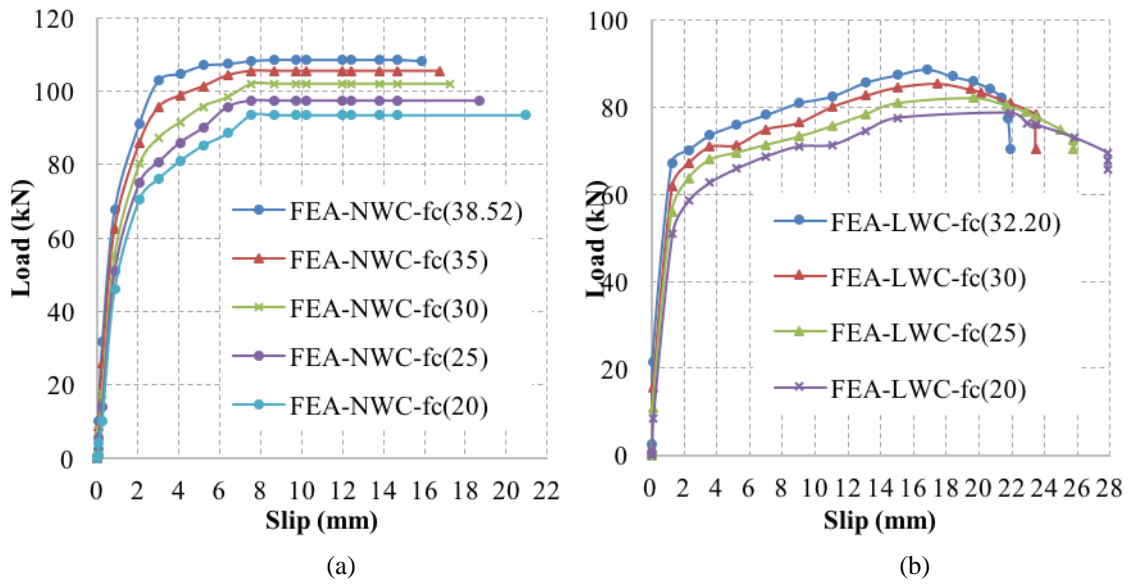
Fig. B-3: Load-slip curves of the FEA with WWSS 22×100mm
with different concrete types
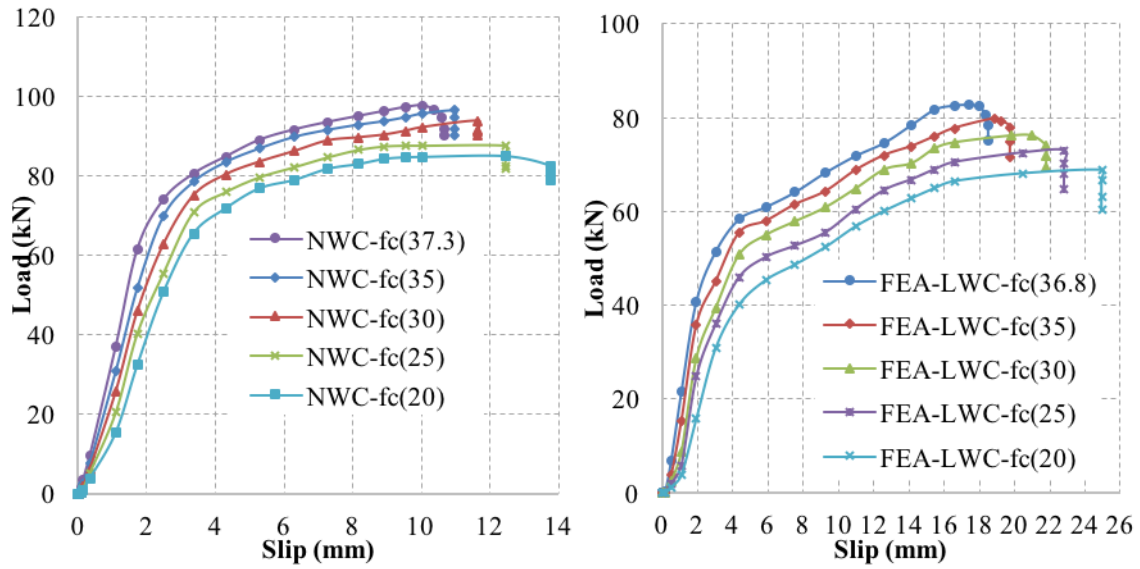
(a)

(b)
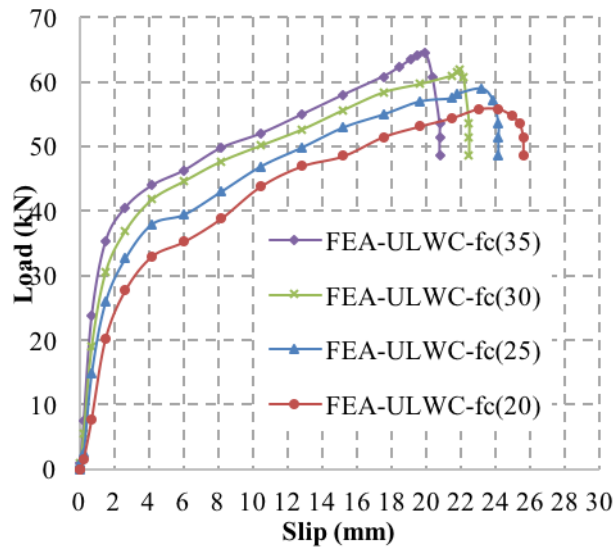
(c)

Fig. B-4: Load-slip curves of the FEA with WWSS with dowels 16mm diameter with different concrete types
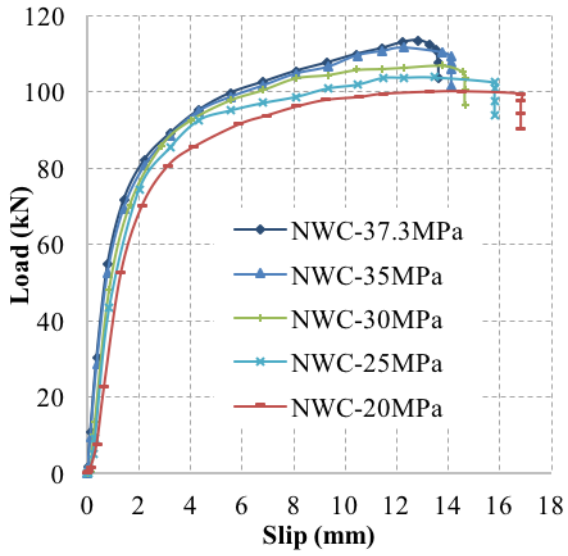
(a)
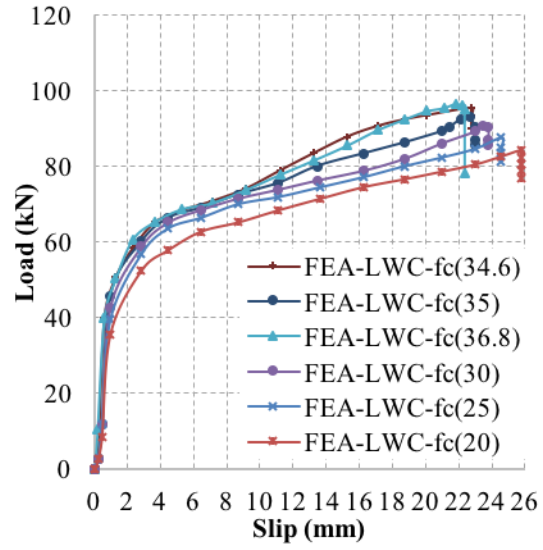
(b)
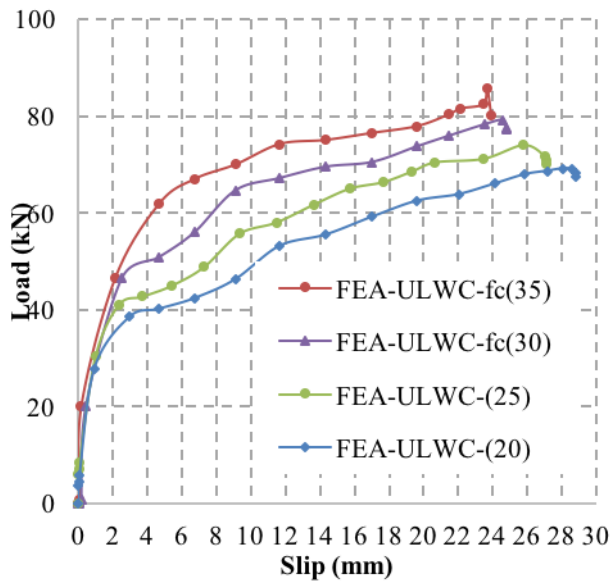
Fig. B-5: Load-slip curves of the FEA with WWSS with dowels 20mm diameter with different concrete types
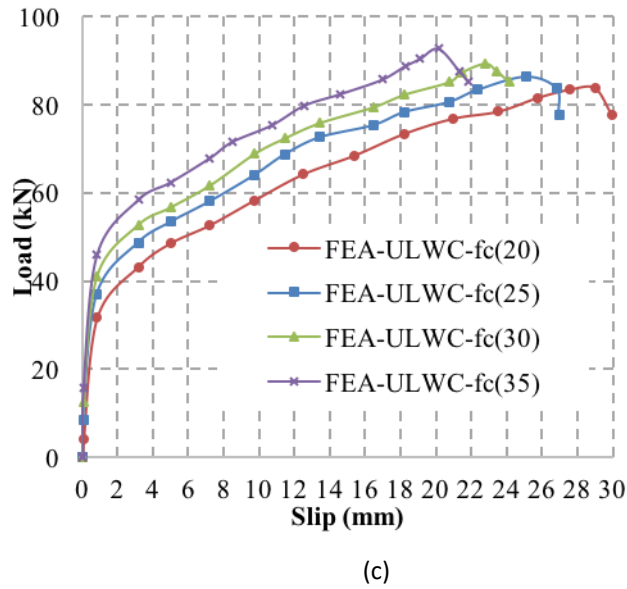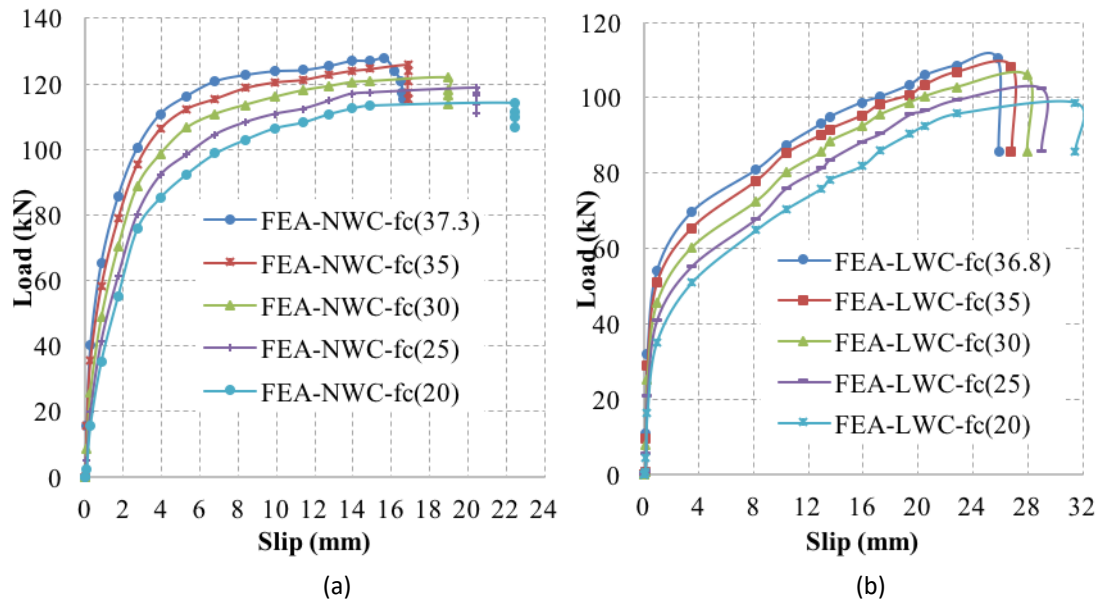
Fig. B-6: Load-slip curves of the FEA with WWSS with dowels 22mm diameter with different concrete types
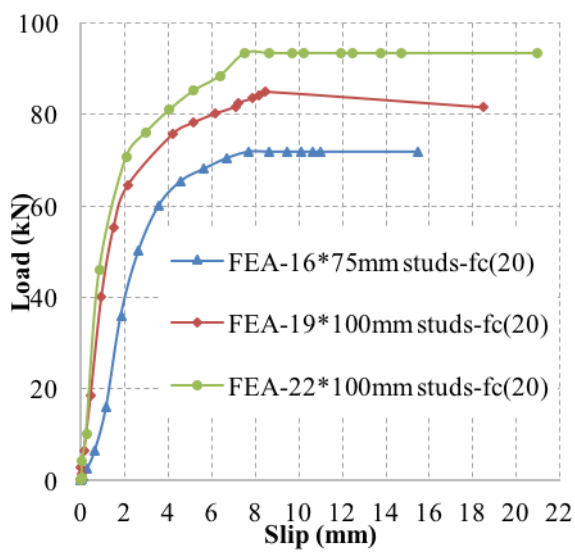
(a): NWC
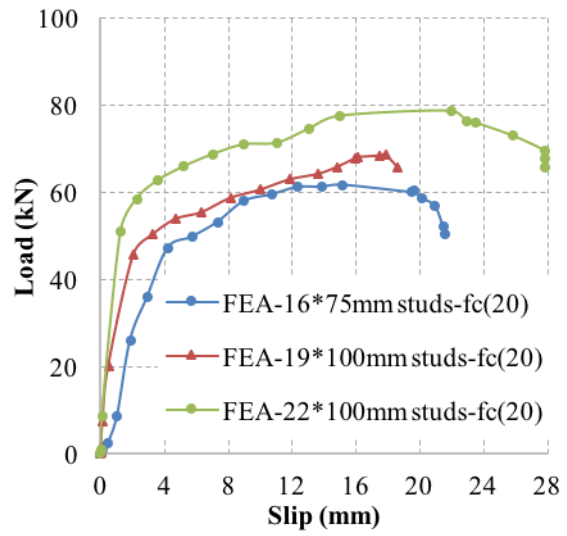
(b): LWC
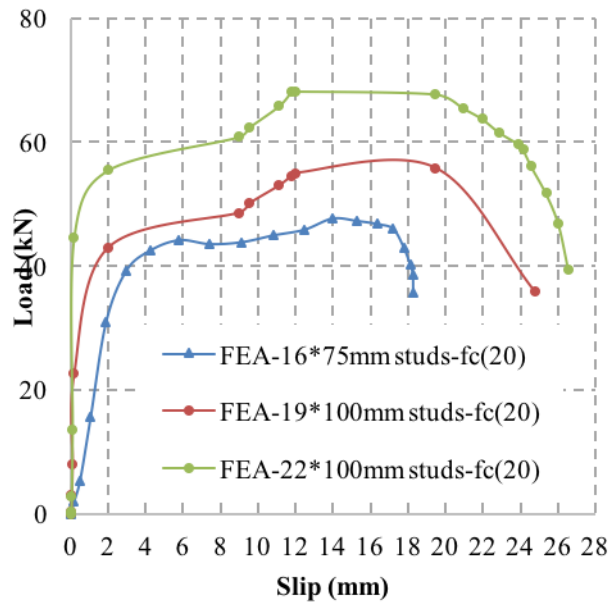
(c): ULWC

Fig. B-7: Load-slip curves of the WWSS FEA with concrete strength of 20N/mm^2 with different stud dimensions

8
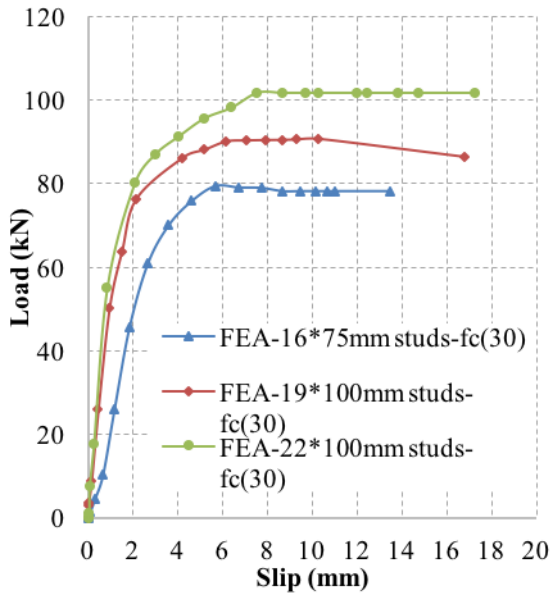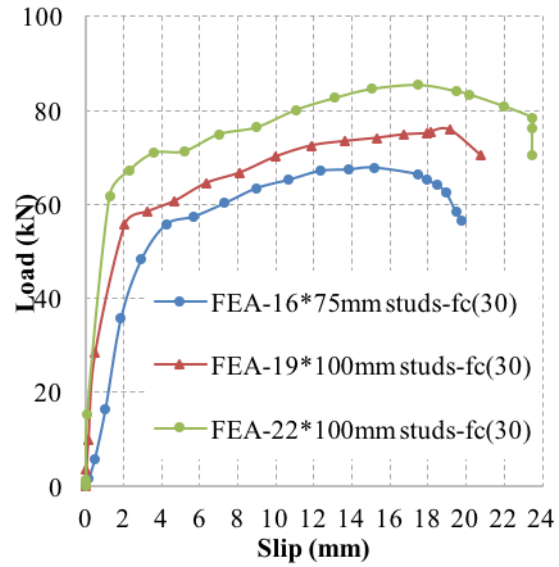
(a): NWC

(b): LWC

(c): ULWC

Fig. B-8: Load-slip curves of the WWSS FEA with concrete strength of 30N/mm^2 with different stud dimensions

9
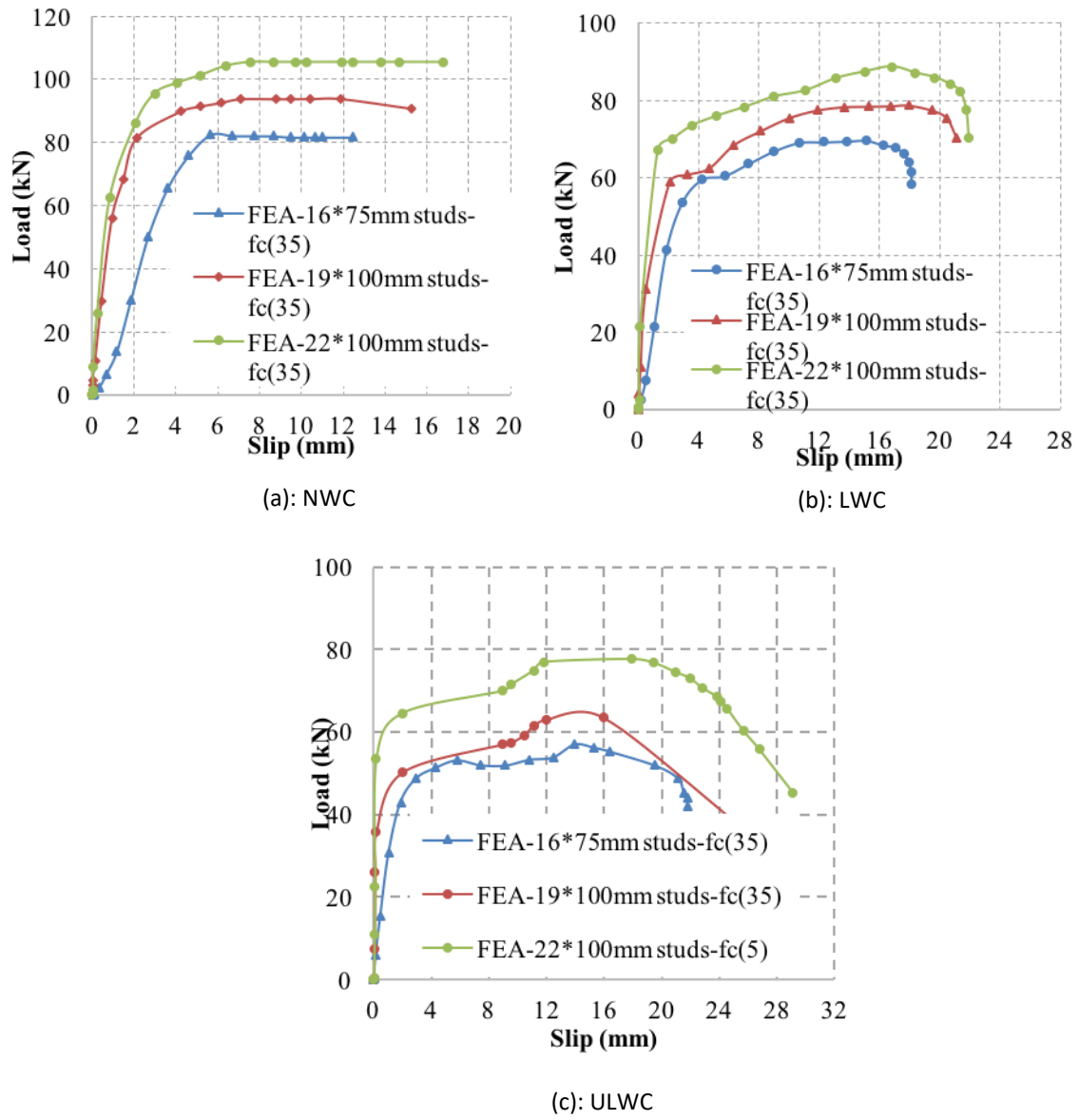
(a): NWC

(b): LWC

(c): ULWC

Fig. B-9: Load-slip curves of the WWSS FEA with concrete strength of 35N/mm^2 with different stud dimensions
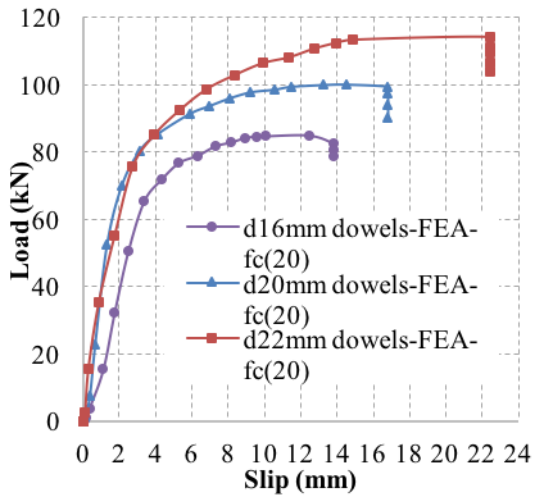
(a): NWC
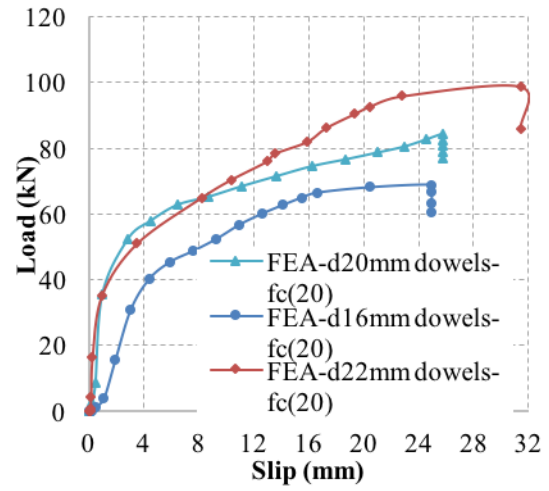
(b): LWC
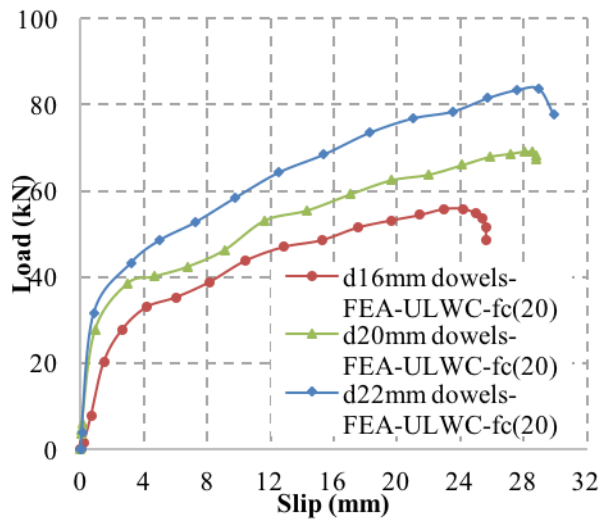
(c): ULWC

Fig. B-10: Load-slip curves of the WWSS with dowels FEA with concrete strength of 20N/mm^2 with different dowel diameters
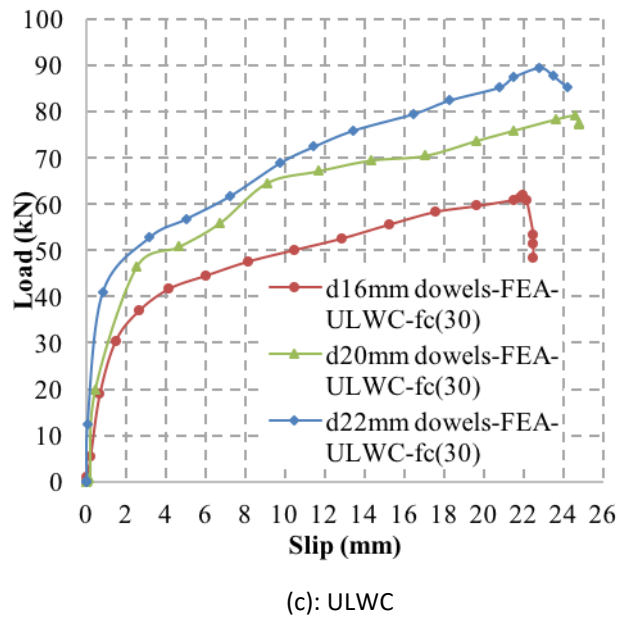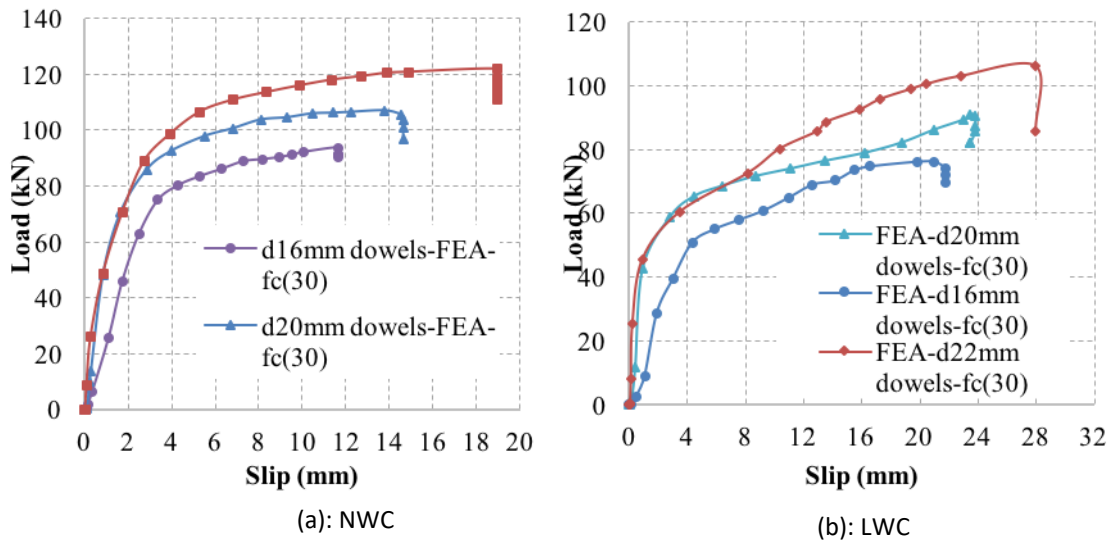
(a): NWC

(b): LWC

(c): ULWC

Fig. B-11: Load-slip curves of the WWSS with dowels FEA with concrete strength of 30N/mm² with different dowel diameters
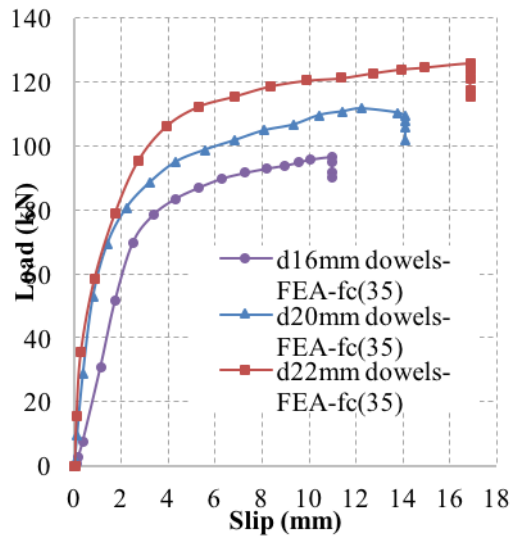
(a): NWC
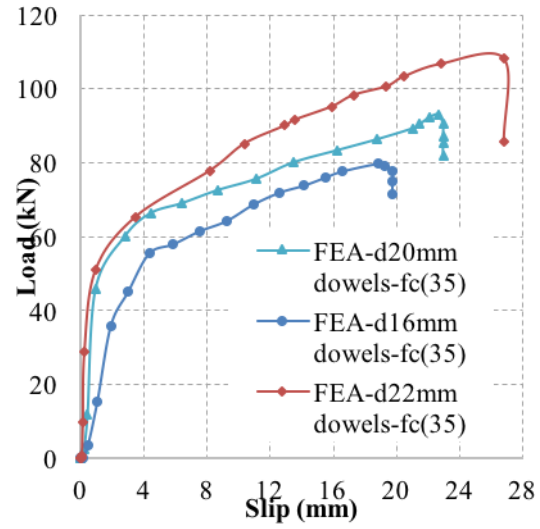
(b): LWC
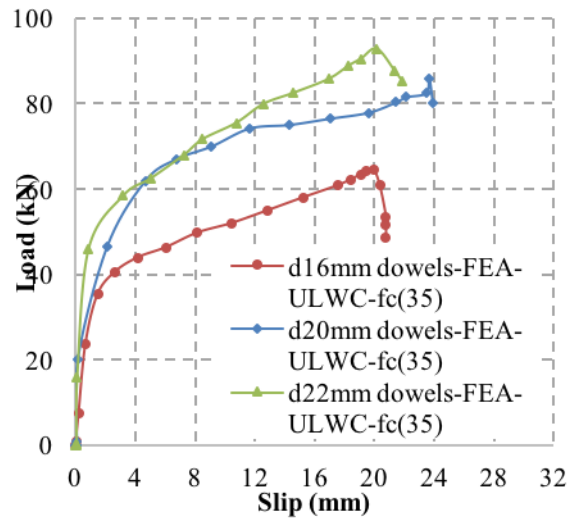
(c): ULWC

Fig. B-12: Load-slip curves of the WWSS with dowels FEA with concrete strength of 35N/mm² with different dowel diameters

13